Mesoporous organosilicas with thiol functionalised pores: multifunctional dendrimers as sacrificial building block and template

Mathilde Laird, Niklas Herrmann, Carole Carcel, Philippe Trens, Erwan Oliviero, Guillaume Toquer, Rozenn Le Parc, Jean-Louis Bantignies, John Bartlett, Michel Wong Chi Man

To cite this version:

Mathilde Laird, Niklas Herrmann, Carole Carcel, Philippe Trens, Erwan Oliviero, et al.. Mesoporous organosilicas with thiol functionalised pores: multifunctional dendrimers as sacrificial building block and template. Nanoscale, 2022, 14 (42), pp.15617-15634. 10.1039/d2nr03097g . hal-03874370

HAL Id: hal-03874370
https://hal.science/hal-03874370v1

Submitted on 28 Nov 2022

Mesoporous organosilicas with thiol functionalised pores:Multifunctional dendrimers as sacrificial building block andtemplate

Mathilde LAIRD,*[a]Niklas HERRMANN,[a]Carole CARCEL,[a]Philippe TRENS,[a]Erwan OLIVIERO,[b]Guillaume TOQUER,[c]Rozenn LE PARC,[d]Jean-Louis BANTIGNIES,[d]John R. BARTLETT*[e]and MichelWONG CHI MAN*[a]

a.ICGM, Univ Montpellier, CNRS, ENSCM, Montpellier, France
b.Univ Montpellier, MEA Platform, Montpellier, France
c.Univ Montpellier, ICSM, ENSCM, CEA, CNRS, Marcoule, France
d.Laboratoire Charles Coulomb (L2C), CNRS-Univ Montpellier, Montpellier, France
e.Western Sydney University, Locked Bag 1797 Penrith NSW 2751 Australia

The synthesis of multifunctional poly(amidoamine) (PAMAM)-based dendrimers containing a cleavable disulfide linkerwithin each armof the dendrimer, together with condensable triethoxysilyl groups on the periphery of the dendrimer, isdescribed. The dendrimers were mixed with bis(triethoxysilyl)benzene and subsequently transformed into silsesquioxanegels or periodic mesoporous organosilicas (PMOs) to generate materials with dendrimers covalently embedded within theinterior of the silsesquioxane networks. Subsequent treatment of the gels with dithiothreitol enabled the core of thedendrimers to be selectively cleaved at the disulfidesite, thus generating thiol functions localised within the pores.The effect of different dendrimer generations on the reactivity of the pendant thiol functions was probed by impregnationwith gold salts, which were reduced to obtain gold nanoparticleswithin the pore networks of the gels and PMOs. The gelsyielded polydisperse gold nanoparticles (2 to 70 nm) with dimensions modulated by the generation of the dendrimer,together with well-defined gold/thiolate clusters with Au...S distances of 2.3 Å. Suchclusters were also observed in the PMOsystem, together with monodispersed gold nanoparticles with diameters comparable to that of the organised pores in thePMO. The role of surface functionalisation in controlling the formation of gold clusters and/or nanoparticles is discusse

1.Introduction

Dendrimers are perfectly defined macromolecules in which thestructure is controlled by an iterative step-by-step synthesis.[1, 2]Eachiteration corresponds to a generation and the properties ofdendrimers are usually driven by their peripheral functions. Sincetheir discovery by Buhleieret al.[3]and the synthesis of dendrimers upto the 10thgeneration by Tomalia et al.[4, 5]in the 1980s, a variety of dendrimer families[6] have been developed including polypropylene-imine,[3, 7, 8] carbosilane,[9] thiosphosphohydrazone[10] and polyamidoamine[4, 5](PAMAM) systems. Dendrimers do not behave as conventional polymers and can exhibit specific properties due to theso-called “dendritic effect”.[11-14] In particular, the properties ofdendrimers can be different from the monomer (“multivalencyeffect”) or different between generations (“generation effect”), leading to a wide variety of applications[2, 15, 16] including drugdelivery/biological applications[17-21]and catalysis,[22-25]with many studies focusing on the PAMAM dendrimer.[26, 27]Owing to their properties, dendrimers have been integrated intosilica-based materials in a variety of ways to produce nanohybrid systems.[28, 29]One ofthe simplest approaches is the direct loading of mesoporous materials with dendrimers. However, this is often limited by the steric hindrance between high-generation dendrimers and the pore apertures.[29, 30]Majoral and co-workers[31] proposed an alternative pathway, where the dendrimer is introduced togetherwith a surfactant template before formation of a silica-based MCM-41 material. Once the MCM-41 framework had condensed, the surfactant was successfully removed while the dendrimer remained (non-covalently) confined within the silica mesopore network. Dendrimers can also be co-condensed or post-grafted on the materials via different strategies such as (a) dendrimer or dendrongrowth on a modified silica[32-34](e.g.,aminopropyl triethoxysilane); (b) post-condensation of trialkoxysilylated dendrimers or dendrons on the free silanol groups of the silica;[35, 36] or (c) the grafting ofpreformed dendrimers on modified silicas[37, 38] (using reactions such as thiol-ene Click, copper catalysed Huisgen addition, etc.). Landskron and Ozin[39] demonstrated the use of trialkoxysilylated dendrimers as precursors to form periodic mesoporous organosilica. The precursors were hydrolysed in the presence of a surfactant and produced a well-defined 2D-hexagonal structure arising from the surfactant, with dendrimers embedded in the walls.The perfectly defined structure of dendrimers also enables them to be used as templates. In 1998, Corriu's group[40] produced, for the first time, xerogels made from carbosilane dendrimers. Carbosilane dendrimers and dendrons were synthesised with trimethoxysilane terminal functions and were employed in a sol-gel process prior to thermal degradation of the organic part of the dendrimer. The materials obtained exhibited a higher porosity than the corresponding material before degradation (250 m^2/g before calcination; 650 m^2/g after calcination) or pure silica (240m^2/g). Although the pore size was inhomogeneous (2-15 nm), probably due to collapse of the structure during calcination, the work provided the first proof-of-concept of the possibility of generating pores using dendrimers. Additional studies by Kriesel and Tilley[41] proved that the specific surface area depends on the size of the dendrimer (generation). Later, Larsen et al.[42, 43] adopted a significantly different approach, in which a generation 4 PAMAM dendrimer template was mixed with tetraethylorthosilicate (TEOS) prior to hydrolysis and condensation of the silane. The dendrimer was not covalently bonded to the silica network and was readily eliminated by calcination. The resulting materials exhibited a specific surface area of around 620 m^2/g with a monodisperse pore size of around 1.5 nm. Wiesner's[44]and Hedrick's groups[45]also developed amphiphilic dendrimers composed of a hydrophilic core and hydrophobic terminal groups. The polycondensation of a silica source in the presence of the templating dendrimers, followed by calcination, led to the formation of well-defined lamellar or hexagonal silica structures. Dendrimers have also been used as templates to promote the formation of mesopores in other sol-gel systems such as titania, where hydrolysis and condensation are more difficult to control.[46]

To date, such "dendrimer-as-template" strategies have not enabled functionalised pores to be directly obtained, since thermal degradation of the template eliminates the organic moieties .Functional pores are generally only obtained by either: (1) co-condensation of an organosilane together with the silica precursor in the presence of a surfactant; or (2) post grafting of organotrialkoxysilanes on preformed porous silica materials.[29] However, the first approach can result in phase segregation or trapping of the organic groups within the silica network (and thus inaccessible for further chemical reactions), while the second can promote inhomogeneous distribution of the functional groups due to diffusion effects (particularly in small pores). Accordingly, the development of strategies to generate functional pores withcontrolled size and distribution of the functional groups is of significant interest.

In this work, we present a general proof-of-concept strategy for the design of new multifunctional dendrimers and their conversion, via sol-gel processing, into materials with functional pendant groups and engineered porosity. Our approach involves the synthesis and characterisation of new multifunctional generation zero (G0) and three (G3) PAMAM-derived dendrimers, which were prepared by grafting a tailor-made cleavable linker onto the arms of the dendrimers followed by the introduction of a condensable triethoxysilyl group on the dendrimers' periphery. The silane was chosen for its capacity to generate an extended silsesquioxane network via sol-gel processing, while the disulfide group was chosen as a cleavable site due to its capacity to be chemically or enzymatically cleaved. In addition, the disulfide cleavage releases achemically reactive thiol function, which can be of particular interest due to its capacity to coordinate a large variety of metals (gold, copper, mercury, etc) and to react with other reagents (such as alkenes via a thiol-ene Click reaction) to provide additional opportunities for post-functionalisation. Transformation of the multifunctional dendrimers into nanohybrid silsesquioxane gels and PMOs (in the presence of Pluronic P123) to generate materials with dendrimers covalently embedded within the interior of the organosilica network is described, together with cleavage of the inner part of the dendrimer to obtain thiol functions localised in the pores. Finally, the reactivity of the pendant thiol functions in botht he gels and PMOs is probed by impregnation of gold salts, which are then reduced to obtain nanoparticles in the confined space created by cleavage of the dendrimer, with the density of thiol functions controlled by the generation of PAMAM used to produce the gels. Although not directly explored in this proof-of-concept study, the generation of pores with controlled size and distribution of functional groups such as thiols opens the way to a variety of application including drug delivery systems,[47] environmentalr emediation and heavy-metal capture,[48] and catalysis,[49] together with other functional pendant groups generated by controlled cleavage of multifunctional dendrimers.

2.Results and Discussion

PAMAM dendrimers are now wide-spread and commercially available in generations ranging from G0 to G11,[50, 51] with a range of surface functional groups that includes $-NH_2$, -OH, -COOH, -COO-, $-Si(OMe)_3$, etc. Hence, they are versatile synthetic platforms for the design and creation of new PAMAM-derived precursors with additional functionality that can be incorporated using conventional modification by organic synthesis techniques, thus avoiding the time and resources required for tedious step-by-step syntheses of new dendrimer types. Such anapproach has been taken in our work by modifying a conventional, commercially available amine-terminated PAMAM dendrimer with a linker bearing an acrylate, a propargyl and a disulfide function (Scheme 1). As shown in Figure 1, the acrylate moiety enables the linker to be grafted onto the NH_2-terminated PAMAM dendrimer using a Michael addition (as used in the PAMAM synthesis), while the alkyne moiety enables triethoxysilylated groups[52, 53] to be introducedviaa CuAAC click reaction. The disulfide moiety offers the possibility of cleaving the inner part of the dendrimer under reducing conditions or by enzymatic catalysis,[47, 54, 55] thus releasing thiol functions, while the triethoxysilylated groups enable the dendrimer to be incorporated in nanohybrid materials *via* sol-gel processing.

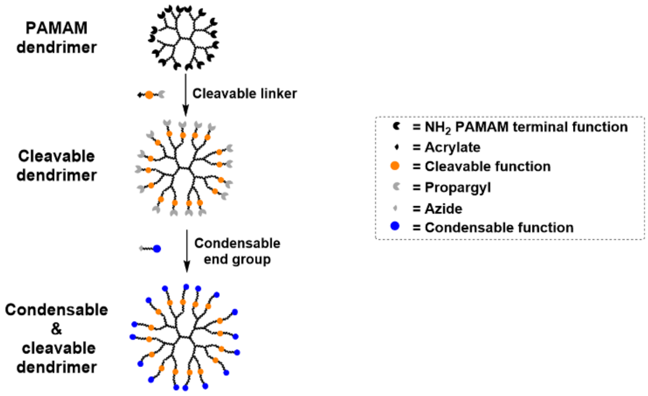

Figure 1 - Schematic representation of the grafting of cleavable linkers to PAMAM

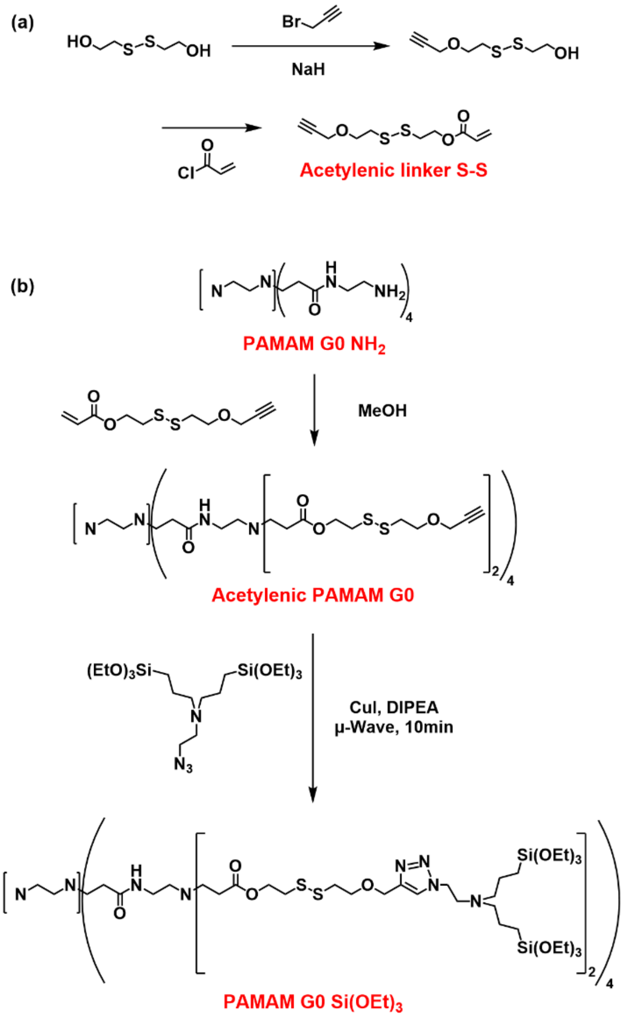

Scheme 1 – Grafting of cleavable linkers to PAMAM

The approach used to construct the multifunctional acetylenic linker is illustrated in **Scheme 1a**, while its subsequent grafting onto the PAMAM dendrimer *via* a Michael addition and CuAAC Click reaction with a bis triethoxysilylated azide compound to obtain the triethoxysilylated cleavable dendrimer is outlined in **Scheme 1b** for the case of the G0 dendrimer. A detailed characterisation study of the intermediates and multifunctional dendrimers is included in the Supporting Information (**Section S3.1**, **Figure S1 to S6**), while the versatility of the multifunctional dendrimers is explored in more detail below.

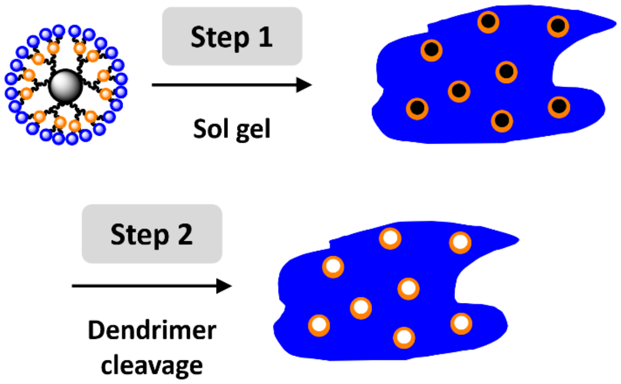

Figure 2 – Synthesis of porous gels with pendant functions

2.1. Gel synthesis and inner dendrimer cleavage

The multifunctional PAMAM-G0-Si(OEt)$_3$ and PAMAM-G3-Si(OEt)$_3$ precursors are readily transformed into gels *via* sol-gel hydrolysis and condensation of the triethoxysilyl groups located on the periphery of the dendrimer molecules (**Step 1** in **Figure 2**). The gels obtained are nanohybrids, consisting of silsesquioxane domains covalently linked to the dendrimer core. Moreover, the dendrimer core itself contains disulfide bonds on each arm of the molecule, which are susceptible to cleavage under controlled conditions. Accordingly, the gels were subsequently treated with dithiothreitol (DTT) to reduce the disulfide bond and cleave the inner part of the dendrimer (**Step 2** in **Figure 2**); this results in the formation of pendant thiol functions in the cavities formed by removal of the PAMAM dendrimer. The thiol functions are thus located in a confined space, with the density of thiols controlled by the dimensions of the pore and the specific dendrimer generation used. DTT was chosen as reducing agent due to its capacity to be eliminated by cyclisation, since alternative reducing agents can remain associated with the material in the form of disulfides. This approach maximises the number of thiol moieties generated while avoiding interference with the reducing agent, with the objective of generating tailored porosity by controlled degradation of the dendrimer.

Two types of material were synthesised, using tetrabutylammonium fluoride (TBAF) as a catalyst. TBAF was selected as a neutral catalyst, to avoid potential hydrolysis of the ester bond of the multifunctional PAMAM dendrimer. The first, synthesised from the pure PAMAM-Si(OEt)$_3$ precursors, will enable the functional groups affected by the DTT treatment to be clearly identified. A second, prepared from a mixture of PAMAM-Si(OEt)$_3$ dendrimer and 1,4-bis(triethoxysilyl)benzene (BTEB), was also synthesised, with dendrimer/BTEB molar ratios of 1/48 and 1/384 for the G0 and G3 systems, respectively. These ratios were chosen to maintain a nominal ratio of one bis(triethoxysilyl) moiety of the dendrimer to six BTEB molecules, with the silsesquioxane structure being consolidated by hydrolysis and condensation of the BTEB precursor. In particular, cleavage of the disulfide bonds and the elimination of a large part of the organic backbone could conceivably lead to the collapse of the structure. **Figure 3** presents a schematic view of the structures expected before and after cleavage of the disulfide bond for PAMAM-G0/BTEB organosilicas.

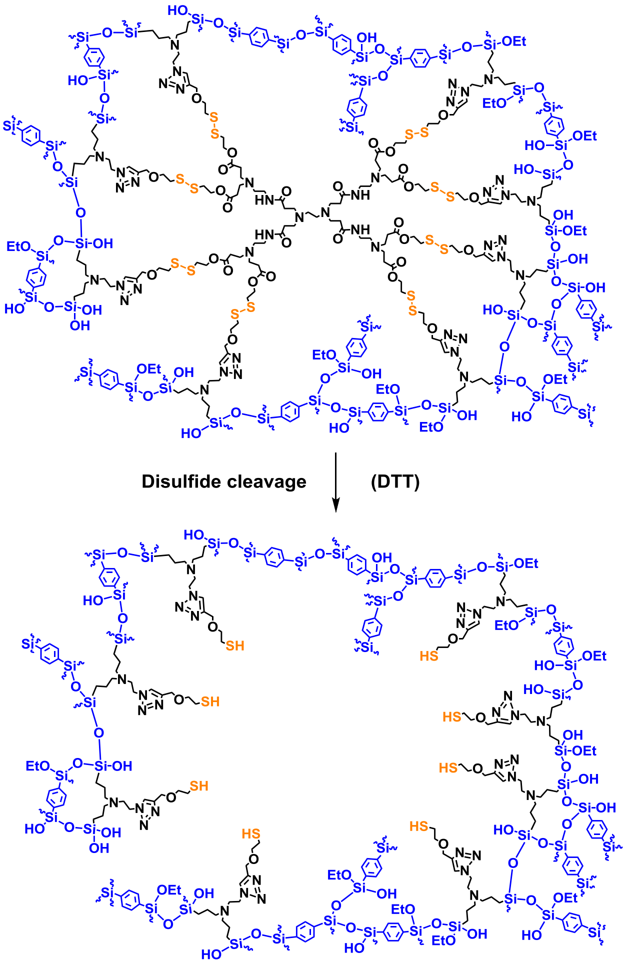

Figure 3 – Structure of gels prepared from PAMAM/BTEB before (top) and after cleavage (wavy bond = Si-O-Si)

2.1.1. Solid state NMR characterisation. **Figure 4** presents the ^{13}C NMR spectra of the gel prepared from pure PAMAM-G0-derived dendrimer before (**a**) and after (**b**) DTT treatment and of the gel prepared from pure PAMAM-G3-derived dendrimer before (**c**) and after (**d**) DTT treatment. The signals at 144 and 124-123 ppm arise from the triazole ring and can, as expected, be found before and after DTT treatment. Indeed, the triazole component, as well as some propyl and ethyl moieties, are the only organic components that should remain after the cleavage of the disulfide bonds. The broad signal cluster corresponding to the PAMAM aliphatic moiety can be observed between 55 and 10 ppm. Due to the numerous features present in this region, the various PAMAM signals cannot be unambiguously attributed. It is noteworthy that the intensity of the aliphatic signals decreases significantly after the DTT treatment of the pure PAMAM-G0 gel (compare

Figure 4 (a) and **(b)**), consistent with loss of the dendrimer core after disulfide cleavage. In the ^{13}C NMR spectra of the gel prepared from pure PAMAM-G3-derived dendrimer before and after DTT treatment (**(c)** and **(d)** in **Figure 4**, respectively), an additional signal arising from the amide groups can be observed at 172 ppm. Although the decrease in the intensity of the aliphatic carbon signals is not as striking as that observed for the G0 system, the diminution of the amide carbons is evident, thus demonstrating the partial removal of the inner part of the dendrimer. These observations are all consistent with cleavage of the inner part of the PAMAM-derived dendrimer.

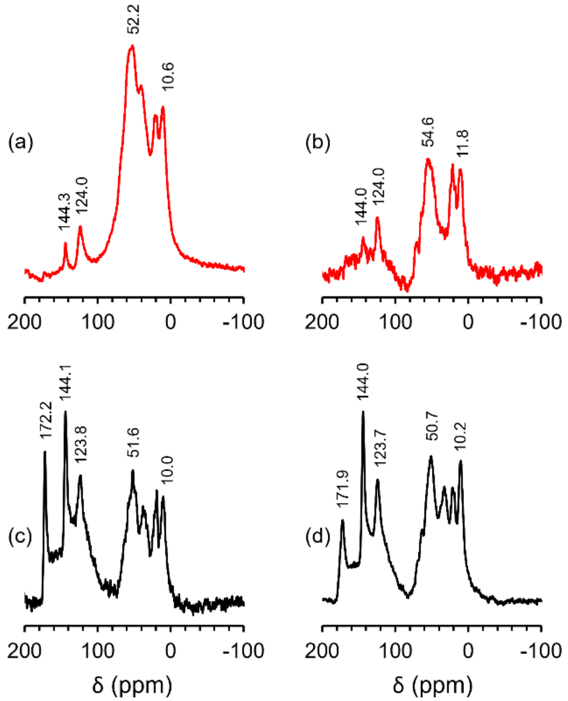

Figure 4 – ^{13}C CP-MAS NMR spectra of pure PAMAM-G0 gel before (a) and after (b) DTT treatment; and of pure PAMAM-G3 gel before (c) and after (d) DTT treatment

Similarly, the results of the ^{13}C solid state NMR study of the gels prepared from PAMAM-Si(OEt)$_3$ precursors and BTEB are presented in **Figure S7** (**a** and **b** for G0; **c** and **d** for G3). The presence of BTEB significantly dilutes the dendrimer, and hence the signals arising from the PAMAM are not clearly observed, with the spectra being dominated by the main signal associated with the BTEB aromatic carbons at 133 ppm. In the PAMAM-G0/BTEB gel, the presence of ethoxy-group signals at 58 and 17 ppm indicates incomplete hydrolysis of the triethoxysilane. The latter signals are not clearly observed in the case of the PAMAM-G3/BTEB gel. Instead, the signals arising from the dendrimer are visible at 144 ppm for the triazole aromatic carbon, 173 ppm for the amide carbon and between 69 and 9 ppm for the aliphatic carbons present in the dendrimer core (**Figure S7, c**). As expected, following DTT treatment, the intensity of the triazole carbon signal observed at 144 ppm remains constant while those of the amide and aliphatic carbon signals decrease (**Figure S7, d**). This observation is consistent with the DTT cleavage of the disulfide bond and the loss of the inner part of the dendrimer.

^{29}Si solid state NMR spectroscopy was also used to compare the structures of the gels before and after DTT treatment, by analysing the integrated intensities of the various signals observed. Since ^{1}H cross-polarisation enhances the intensity of the signals from silicon atoms with neighbouring protons,[56, 57] care must be taken with such interpretations. However, although the CP-MAS measurement cannot be considered quantitative, it is reasonable to compare relative signal intensities between samples derived from the same materials and bearing identical organic groups near the various silicon sites. In this way, variations in the relative abundances of the different sites within the gels can be compared. In addition, in the case of bridged silsesquioxanes, the CP-MAS analysis has previously been found to be quite representative of the relative abundances in such systems.[58]

Figure S8-S11 and **Table S1-S4** present the fitted ^{29}Si solid state NMR spectra of the materials prepared from the dendrimers and the attribution of the fitted signals to the different T^{n} aliphatic/aromatic silsesquioxane sites (see discussion in **Section S3.2** of the Supporting Information). These data reveal that DTT treatment does not impact significantly on the extent of condensation in the materials.

2.1.2 Chemical composition: infrared and Raman spectroscopy.

To further probe the molecular-scale structure of the materials, complementary FTIR and Raman spectra were acquired to provide additional insights into the functional sites present in the molecules. **Table S5** summarises the wavenumber and attributions (based on the spectra of model compound) of key diagnostic modes of functional groups present in the multifunctional PAMAM-derived precursors and BTEB, which were used for assigning bands in the vibrational spectra of the

PAMAM/BTEB gel systems. A detailed analysis of the spectra of selected model compounds was also undertaken, to enable the bands of interest in the materials to be identified, together with the most appropriate spectroscopic method for their characterisation; these data are also summarised in **Table S5**.

The FTIR spectra of the PAMAM-G0 and -G3 gels before and after DTT treatment are shown in **Figure 5**. Since the corresponding ^{29}Si NMR data indicated that the extent of condensation in the gels was not significantly impacted by DTT (see **Section S3.2** in the Supporting Information), the spectra were normalised against the intensity of the respective Si-O-Si stretching modes around 1100 cm^{-1}. Striking changes are evident after DTT treatment, including a substantial decrease in the intensity of the ester ν(C=O) modes at 1736 and 1729 cm^{-1}, as well as the amide I modes of the PAMAM skeleton at 1653 and 1646 cm^{-1} for G0 and G3 dendrimers, respectively (**Figure 5(a)**). The decrease in the intensity of the amide II stretching mode at 1548 cm^{-1} is also clearly evident for the PAMAM-G0 gel. These observations are consistent with cleavage of the dendrimer core. In addition, integration of the carbonyl signals before and after DTT treatment suggests that 85 % of the dendrimer core is removed in the case of the PAMAM-G0 gel and around 45% in the case of the PAMAM-G3 gel. The difference in the extent of dendrimer removal can be explained by the larger number of branches to be cleaved to remove the G3 dendrimer compared to the G0 system. Furthermore, the larger size of the G3 dendrimer would be expected to hinder its diffusion in the silica network.

Similarly, the loss of the $\nu_{as}(CH_3)$ and $\nu_s(CH_3)$ bands is evident by comparing the spectra of the PAMAM gels and the corresponding precursors (**Figure S12 a** and **b**), indicating essentially complete hydrolysis in the gels, as discussed above. Interestingly, the overall decrease in the intensity of the CH_2 stretching-mode profiles between 2800 and 3000 cm^{-1} in the spectra of the gels before and after DTT treatment (**Figure S12 a** and **b**) is consistent with the loss of the inner part of the dendrimer. Around 40 % of the total CH_2 intensity is expected to disappear following complete DTT cleavage. However, as the observed decrease in the intensity of the C=O stretching band indicated only partial removal of the dendrimer core, the decrease of the CH_2 stretching band intensity is completely consistent with partial cleavage of the dendrimer.

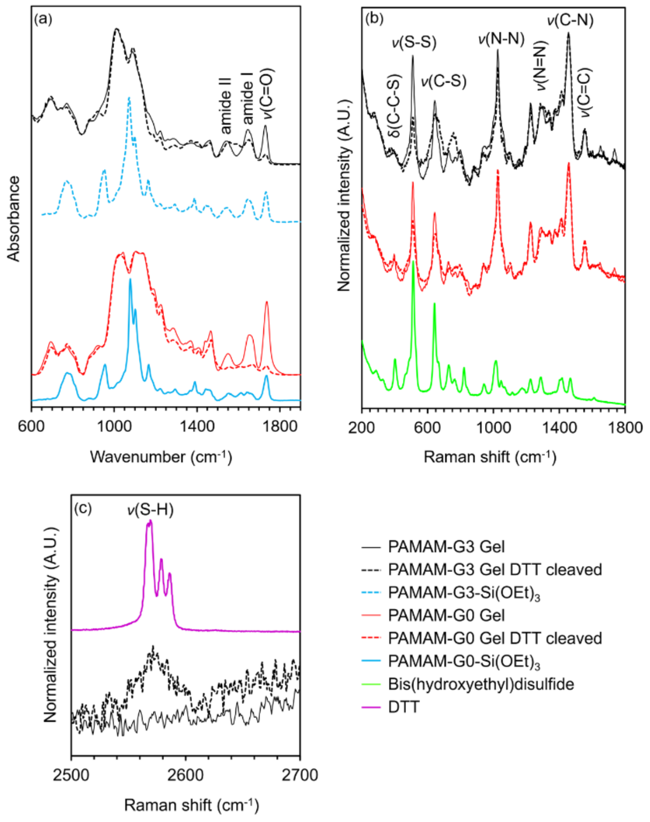

Figure 5 – (a) FTIR spectra of PAMAM-G0-Si(OEt)$_3$ (cyan, solid line), PAMAM-G3-Si(OEt)$_3$ (cyan, dotted line) and of the PAMAM-G0 (red line) and PAMAM-G3 gels (black line) before (solid line) and after DTT cleavage (dotted line). (b) Corresponding Raman spectra, including bis(hydroxyethyl)disulfide (green line). (c) Raman spectra (including DTT, violet line) illustrating the formation of -SH species in the PAMAM-G3 gel following DTT cleavage. Note that a moving-average smoothing function was applied to the Raman data to reduce noise

Raman spectroscopy provides a complementary approach for investigating the vibrational spectra of molecules, and the Raman spectra of the gels, before and after DTT treatment, are included in **Figure 5(b)** (200 to 1800 cm^{-1}) and **Figure 5(c)** (2400 to 2700 cm^{-1}). The spectra were normalised against the intensity of the triazole modes at 1028 (ν(N-N)), 1228 (ν(N=N)), 1296 (ν(N=N) and ν(C-N)), 1343 (in-plane ring stretching), 1460 (ν(C-N)) and 1555 cm^{-1} (ν(C=C)), since the triazole moiety is present before and after cleavage. The spectra of relevant model compounds bearing S-S and C-S bonds are also included in **Figure 5** and **S12** for comparison (bis(hydroxyethyl)disulfide and DTT, respectively).

The data in **Figure 5(b)** reveal that the intensities of ν(S-S) (~510-513 cm^{-1}) and of the disulfide C-S stretching modes, ν(C-S) around 640 cm^{-1} are significantly reduced in both the G0 and G3 gels after DTT treatment. To a lesser extent, the decrease of intensity of δ(C-C-S) at 400 cm^{-1} is also visible in the PAMAM-G0 gel. The expected evolution of ν(S-H) at 2572 cm^{-1} in the PAMAM-G3 gel, although not visible in IR, is also observed following DTT treatment (**Figure 5(c)**). However, the corresponding mode could not be observed in the PAMAM-G0 spectra. When considered in conjunction with the decrease in the intensity of the disulfide bands, the appearance of the thiol band clearly demonstrates the successful cleavage of the disulfide bond and the associated formation of the thiol functions in the gel.

The FTIR spectra of the PAMAM-G0/BTEB and PAMAM-G3/BTEB gels, **Figure S13** (normalised against the Si-O-Si modes) reveal similar trends to those described above for the corresponding PAMAM gels. In particular, a pronounced decrease in the intensity of ν(C=O) at 1736-1729 cm^{-1} is evident for both the G0 and G3 systems (**Figure S13 a** and **b**) after DTT treatment, consistent with cleavage of the inner core of the dendrimer. As expected, a concomitant decrease in the intensity of the amide I and II modes is also observed.

The Raman spectra of the gels, normalised against the ν(C=C) mode of BTEB at 1601 cm^{-1} (which is not affected by the DTT cleavage), are shown in **Figure S13 c** and **d**). Although the spectra are clearly dominated by the modes arising from the BTEB, a clear decrease in the intensity of ν(S-S) at ~510 cm^{-1} can be seen after DTT treatment, demonstrating partial cleavage of the dendrimer. Unfortunately, ν(C-S), at 635 cm^{-1}, appears at the same position as the in-plane ring deformation of the BTEB, and hence the former band cannot be used to corroborate the result.

The vibrational spectra described above are all consistent with significant cleavage of the disulfide bond and loss of the inner part of the PAMAM-derived dendrimer following DTT treatment of the materials.

2.1.3 Textural properties of PAMAM gels.

A key goal of this work was the formation of materials with functionalised porosity obtained by the controlled cleavage of the disulfide linkers incorporated within the materials, and hence the gels obtained from the PAMAM-Si(OEt)$_3$ dendrimer were characterised by TEM, N_2 physisorption and SWAXS to determine their textural properties. No open porosity was observed in the case of the PAMAM-G0 or PAMAM-G3 gels either before or after dendrimer cleavage by N_2 physisorption. Similarly, no organisation of the porosity could be detected by SWAXS. The lack of organisation is not surprising, as there is no obvious driver to promote large-scale dendrimer organisation. TEM measurements of the samples prepared by microtomy show dense materials before and after cleavage, with no evidence for the creation of porosity. The absence of visible porosity created by the removal of the inner part of the dendrimer, as demonstrated by vibrational spectroscopy, is tentatively attributed to collapse of the PAMAM gel structure due to the removal of a large part of the organic framework and the low mechanical strength of the inorganic domains.

In the case of gels prepared from PAMAM-Si(OEt)$_3$ dendrimer/BTEB mixtures, a mixed Type I/IV sorption isotherm is observed for both the G0 and G3 systems prior to cleavage of the disulfide bond (**Figure 6 (a) and (b), solid lines**). These materials are therefore heterogeneous in terms of textural properties. In both cases, the sorption isotherms exhibit a steep slope at low relative pressures and reach a saturation plateau after a rather linear increase in the adsorbed amount. The first feature is typical of microporous materials, whereas the saturation, observed here for p/p° ~ 0.7, reveals the completion of mesopore filling. The distinction between micropore and mesopore filling domains is not easy to define, as these sorption processes overlap. However, it can be concluded that these materials are composed of large micropores (diameter above 1 nm) and a wide range of mesopores ranging from 2 to 7 nm. This can be better seen in **Figure S14** where the pore size distributions are presented. Beyond these common observations, it is noteworthy that the respective saturation plateaus are quite different. In the case of the PAMAM-G0/BTEB gel, saturation is observed at 143 cm^3.g^{-1} whereas it is more than twice as high for PAMAM-G3/BTEB gel (310 cm^3.g^{-1}). These values correspond to pore volumes of 0.22 and 0.48 cm^3.g^{-1}, respectively, as reported in **Table 1**. Focusing on the G0 analogue, the rather small pore volume is principally located in the mesopores (82%), whereas in the case of the G3 analogue, the large pore volume originates from both micropores (30%) and mesopores (70%), with the microporosity attributed to cavities in the dendrimer structure.[59, 60]

The DTT cleavage has an obvious impact on the properties of the final materials, due both to the removal of some organic mass (which increases the measured surface area and porosity on a "per gram" basis) and to the creation of voids. Even though the shapes of the sorption isotherms are very similar upon DTT cleavage (**Figure 6 (a) and (b), dashed lines**), this cleavage operates in different ways between the G0 and G3 analogues, because the original materials are different. DTT cleavage results in a significant increase of the small mesopores population as cavitation at p/p°=0.42 is much more pronounced in the cleaved materials (**Figure S14**). [61] Additionally, a small population of larger mesopores can be found up to 7 nm. Cleavage increases this population for both materials to a small extent. A more detailed analysis of the isotherms shows that for the PAMAM-G0/BTEB gel, micropores have almost disappeared (from 0.04 down to 0.02 cm^3.g^{-1}) after DTT treatment. On the other hand, the total pore volume has increased significantly (from 0.22 up to 0.59 cm^3.g^{-1}) because of the formation of mesopores (see **Table 1**). These are heterogeneous, as denoted by the large quantities of N_2 physisorbed at intermediate relative pressure before the saturation plateau is reached at p/p° = 0.8. These observations are consistent with significant porosity following DTT treatment, mainly resulting from the formation of mesoporosity. Accordingly, the specific surface area of the G0 analogue increases from 361 to 817 m²/g upon DTT treatment. Additionally, the heterogeneity and absence of organisation of the pores was confirmed by TEM imaging and SWAXS measurements, which exhibited featureless scattering curves. In the case of the G3 analogue, beyond the similarity with the sorption isotherm obtained with the cleaved G0 analogue, the most surprising feature upon DTT cleavage is the observed decrease of the specific surface area, despite the fact that organic moieties have been removed from the original G3 material. From **Table 1**, it can be seen that the DTT cleavage leads to a large increase in the mesopore volume (from 0.31 to 0.54 cm^3/g) at the expense of the micropores (from 0.15 to 0.02 cm^3.g^{-1}). This latter observation is consistent with the loss of the inner part of the dendrimer upon cleavage, as microporous cavities are present in the G3 dendrimer itself. However, micropores are an important contributor to the total pore volume and the specific surface area of the original G3 material. These two effects compete, and while the overall specific pore volume increases due both to the prominent role of the mesopores and the decreasing mass of the material, the specific surface area decreases because of the disappearance of the micropores upon cleavage. TEM observations and SWAXS measurements are both consistent with the absence of organised porosity.

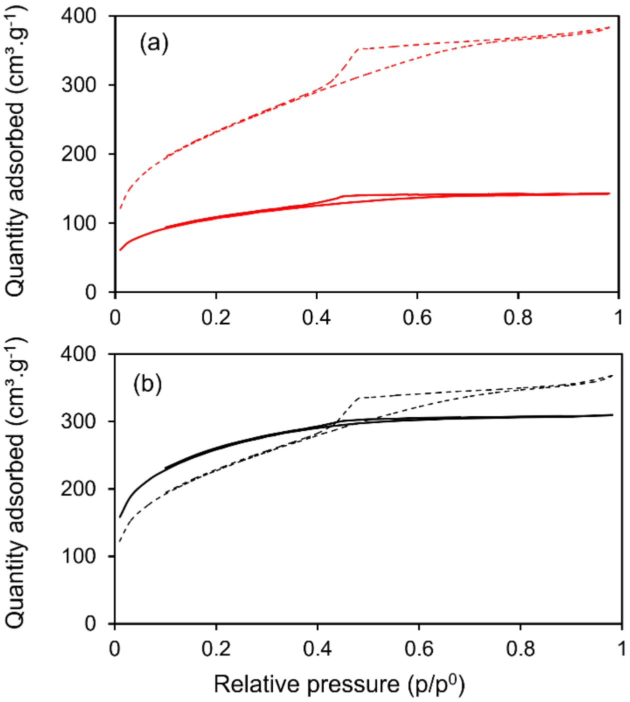

Figure 6 – N_2 physisorption isotherms of (a) PAMAM-G0/BTEB and (b) PAMAM-G3/BTEB gels before (solid lines) and after (dashed lines) DTT cleavage

Table 1 - Selected textural properties from N_2 physisorption analysis of PAMAM-G0/BTEB and PAMAM-G3/ BTEB before and after DTT cleavage

Gel	BET SA* ($m^2.g^{-1}$)	Total PV** ($cm^3.g^{-1}$)	Micro PV ($cm^3.g^{-1}$)	Meso PV ($cm^3.g^{-1}$)
G0/BTEB	361	0.22	0.04	0.18
G0/BTEB, cleaved	817	0.59	0.02	0.57
G3/BTEB	846	0.48	0.15	0.33
G3/BTEB, cleaved	793	0.56	0.02	0.54

* SA : surface area, ** PV : pore volume

Gels obtained by sol-gel processing of BTEB typically exhibit mesoporosity,[62] and BTEB gels synthesised in our laboratory under conditions similar to those used to prepare the dendrimer gels also exhibited (unorganised) mesoporosity. Hence, an important contribution to the porosity observed before DTT cleavage could arise from gelation of the BTEB precursor in THF. These results confirm the important role of BTEB in enhancing the mechanical strength of the nanohybrid gels, by preventing collapse of the gel network during cleavage of the disulfide bonds and subsequent loss of the dendrimer core. As mentioned above, there is a significant increase in pore volume upon cleavage of the dendrimer core (**Table 1**). However, although there are clear differences in the textural properties of the materials prior to cleavage, it is intriguing to observe that after cleavage, the shapes of the nitrogen physisorption isotherms are almost independent of the initial dendrimer generation (**Figure 6 (a) and (b), dashed lines**). This suggests that the size of the dendrimer does not impact significantly on the size or shape of the pores in the cleaved gels, despite a two-fold difference in the radii of the G0 (< 7 Å) and G3 dendrimers (~14 Å).[59] To interpret this interesting and unexpected effect, we note that the core region of the PAMAM dendrimer is hydrophilic while BTEB is hydrophobic, and it is anticipated that BTEB molecules would be largely excluded from the interior of the PAMAM dendrimer in the gel precursor solutions. Hence, the initial hydrolysis of the BTEB and silylated dendrimers will occur in nano-sized domains composed largely of BTEB and dendrimer, with the proportions of BTEB being more than three times higher than that of the dendrimer. It has been reported that the rate of hydrolysis of R-Si(OMe)$_3$ compounds is higher in the case of aromatic substituents (R = phenyl) than for aliphatic substituents such as n-propyl or 3-methacryloxypropyl.[63] Hence, it can be assumed that the rate of hydrolysis of BTEB would be higher than that of the silylated PAMAM. Consequently, the formation of a silsesquioxane framework arising from BTEB monomers is expected to occur at a faster rate than that of the corresponding PAMAM species, leading to entrapment of the condensing PAMAM species within a predominantly BTEB-derived network.

The initial BTEB/dendrimer gels obtained would thus consist of G0 or G3 dendritic networks filling the pores of the BTEB-derived network, with the corresponding N_2 physisorption isotherms (**Figure 6** and **Table 1**) mainly probing the porosity of the confined PAMAM networks. As mentioned previously,[59, 60] increasing the size of PAMAM dendrimers leads to a corresponding increase in the internal void volume, and hence the higher pore volume of the BTEB/G3 product before DTT cleavage is not unexpected. Subsequent cleavage of the disulfide linkages releases the dendrimer core from the gels, liberating the mesoporosity mainly associated with the BTEB gel framework. After this treatment, the textural features of the BTEB/G0 and BTEB/G3 gels appear quite similar (**Figure 6** and **Table 1**). However, although the total disulfide content in the PAMAM-G0/BTEB and PAMAM-G3/BTEB gels is nominally comparable prior to cleavage, each G3 molecule contains eight times as many disulfide linkages as the G0 system. Hence, the surface distribution of thiol functions following cleavage would be expected to be different, with the pores in the G3 system featuring regions with more densely packed surface thiols than in the corresponding G0 system. This feature of the gels will be explored in more detail below.

2.1.4 Impregnation with Au(III) salts and formation of Au(0) nanoparticles.

The formation of gold nanoparticles within the mesoporous PAMAM dendrimer/BTEB gels was investigated by impregnating the DTT-treated gels with a $NaAuCl_4$ solution, with subsequent reduction by $NaBH_4$ (**Section S2.4** of the Supporting Information). The procedure involved two iterations of impregnation/washing/reduction/washing cycles, with the washing steps minimising the retention of non-coordinated gold salts on the materials and their transformation into metallic gold nanoparticles. A gel prepared from pure BTEB using a similar synthesis procedure was used as a control and was impregnated under the same conditions.

Representative TEM images of the Au nanoparticles in the pure BTEB, PAMAM-G0/BTEB and PAMAM-G3/BTEB gels are illustrated in **Figure 7**, while the corresponding size distributions are shown in **Figure 8**. EDX elemental maps and spectra are given in **Figure S16** and **S17**, respectively. The Au/Si mole ratios obtained from EDX spectra recorded in three different regions of the samples are summarised in **Table 2**. Due to the substantial overlap between the sulfur peak (2.30 keV) and the various gold peaks (2.13, 2,22 and 2.42 keV) in the EDX spectra, the EDX software could not obtain meaningful analyses of the sulfur content in the PAMAM-G0/BTEB and PAMAM-G3/BTEB samples and hence these data are not included in **Table 2**.

Table 2 - Selected atomic ratios obtained by TEM-EDX for BTEB, PAMAM-G0/BTEB and PAMAM-G3/BTEB gels

Gel	Au:Si atomic ratios obtained from difference sampling regions		
BTEB	0.033	0.069	0.074
PAMAM-G0/BTEB	0.066	0.088	0.264
PAMAM-G3/BTEB	0.354	0.355	0.595

The obvious differences in the gold content, number of visible gold nanoparticles and the corresponding size distributions for the PAMAM-G0/BTEB and PAMAM-G3/BTEB samples are striking and suggests potential differences in the sulfur/thiol content and/or the distribution of thiol species between the two samples. The pristine PAMAM-G0/BTEB and PAMAM-G3/BTEB gel samples were synthesised using comparable R-S-S-R`:Si mole ratios, suggesting that the nominal S:Si mole ratios in the samples should be comparable after the washing/impregnation cycles. As discussed above, it is not possible to directly obtain the S:Si atomic ratios from the EDX data. However, differences in the S:Si mole ratios can be explored by curve fitting of the EDX spectra to subtract the contributions of the gold peaks to the EDX spectral profiles (**Section S3.2** of the Supporting Information). The approach used is illustrated in **Figures S18**, **S19** and **S20**. Weighted subtraction of the reconstructed Au spectrum from those obtained from two different regions of the impregnated PAMAM-G0/BTEB and PAMAM-G3/BTEB samples, **Figure S20**, clearly reveals a two-to-threefold difference in the S:Si atomic ratios between the G3 and G0 systems. This difference is correlated with the larger Au content observed in the PAMAM-G3/BTEB system (**Table 2**), consistent with the expected role of thiol species in complexing Au(III) and mediating the subsequent formation of Au nanoparticles during treatment with $NaBH_4$.

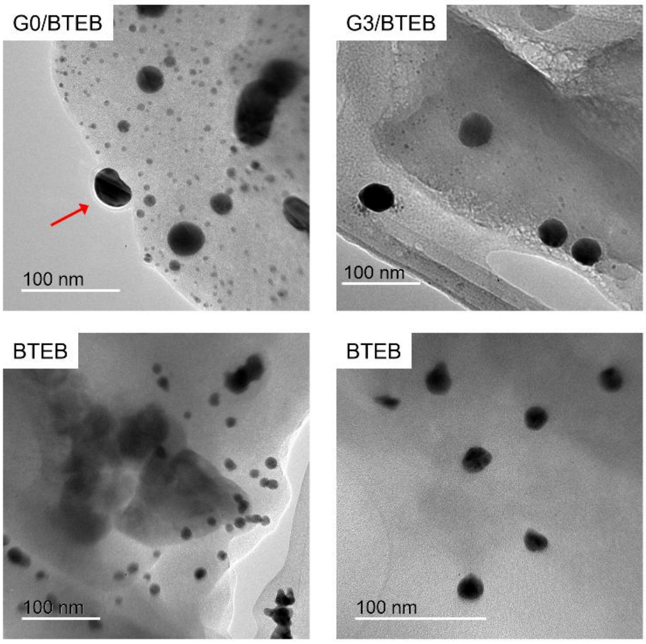

Figure 7 - Representative TEM images of Au nanoparticles in PAMAM-G0/BTEB, PAMAM-G3/BTEB and pure BTEB gels. The red arrow shown in the top-left image indicates a nanoparticle that has grown outside of the silsesquioxane mesopore network

The differing Au content and S:Si atomic ratios between the PAMAM-G0/BTEB and PAMAM-G3/BTEB gels is intriguing, given that the sulfur content in the two systems is essentially identical prior to cleavage. We note that the FTIR data discussed above indicate that the extent of cleavage in the case of the PAMAM-G0/BTEB is around 85 % following DTT treatment, compared to 45 % in the PAMAM-G3/BTEB system. The loss of each arm from the dendrimer core will generate one thiol group bound to the silsesquioxane framework and lead to the removal of one thiol moiety attached to the cleaved arm. Hence, assuming complete retention of the dendrimer periphery *via* condensation with the framework, 85 % of the initial disulfide linkages present in the PAMAM-G0/BTEB system will contribute one surface thiol moiety after DTT treatment, while 15 % will be retained as disulfides. In the case of the PAMAM-G3/BTEB system, 45 % of the initial disulfide linkage initially present will contribute one surface thiol, with 55 % being retained as disulfides. The corresponding ratio of the sulfur contents in the two systems would thus be expected to be around 1.3, which is much smaller than the ratio of 2-3 obtained from the semi-quantitative EDX analysis. One possible reason for this discrepancy is that the reaction between the R-Si(OEt)$_3$ sites on the PAMAM dendrimer and the silsesquioxane framework formed by hydrolysis and condensation of BTEB may be incomplete, which is consistent with the presence of signals arising from T^1 and T^2 species in the ^{29}Si solid state NMR spectra (**Figure S10** and **S11**). In the case of the PAMAM-G0 molecule, at least one of the 16 silylated arms on each PAMAM must undergo condensation to ensure retention of the PAMAM within the network. In contrast, for the PAMAM-G3, only one of 132 silylated branches must condense to retain the PAMAM in the silica network. Consequently, even with incomplete condensation, the PAMAM-G3 has a higher probability of being retained. In addition, the relatively small unbound PAMAM-G0 species can diffuse from the mesoporous network in the silsesquioxane matrix during the extensive washing process. In contrast, the substantially larger PAMAM-G3 species would be more easily retained within the network, even if they were not covalently bound to the framework.

Although both the S and Au content in the PAMAM-G3/BTEB sample are higher than those of the corresponding G0 system (**Table 2**), fewer small nanoparticles are observed in the former case under the conditions used to acquire the micrographs in **Figure 7** with the data revealing marked differences in the apparent number and size distribution of Au nanoparticles in the various samples (**Figure 7** and **8**). The Au nanoparticles in the BTEB gel exhibit a broad bimodal size distribution, with maxima around 5 and 15 nm. Not surprisingly, the EDX analyses indicate that the corresponding Au content is the lowest of all the samples, due presumably to the lack of surface thiol functions to complex and retain the impregnated Au(III) species prior to washing and reduction. The PAMAM-G3/BTEB gel also exhibits a bimodal size distribution, with maxima around 5 and 40 nm. For both of these samples, the larger nanoparticles are clearly evident in the corresponding TEM micrographs (**Figure 7**). However, the Au content in the PAMAM-G3/BTEB samples is substantially higher than that of the BTEB sample (**Table 2**), as expected given the presence of thiol moieties to complex impregnated Au(III) species in the former case.

The quantity of Au in the PAMAM-G0/BTEB sample is intermediate between that of the pure BTEB and PAMAM-G3/BTEB samples (**Table 2**). The former sample exhibits a broad size distribution with a maximum around 4-5 nm. Although a small number of larger Au nanoparticles are evident, the TEM micrograph in **Figure 7** clearly illustrates the significantly larger number of smaller nanoparticles compared to the BTEB and PAMAM-G3/BTEB gels. The larger particles presumably arise from reduction of the non-coordinated Au(III) salt retained after washing, whereas those ranging from 2 to 6 nm are attributed to nanoparticles formed by reduction of gold salts coordinated to the pendant thiol functions, with the proximity of adjacent thiol functions (dendritic effect) determining the size of the particles by stabilising them against aggregation.

In all cases, the larger Au nanoparticles observed in **Figure 7** are much larger than the mesopores present within the silsesquioxane network. This suggests that these particles are formed either (a) by diffusion of smaller Au species initially generated within the mesopore network to the external surface of the gel and subsequent coalescence; or (b) directly on the external surface of the silsesquioxane matrix.

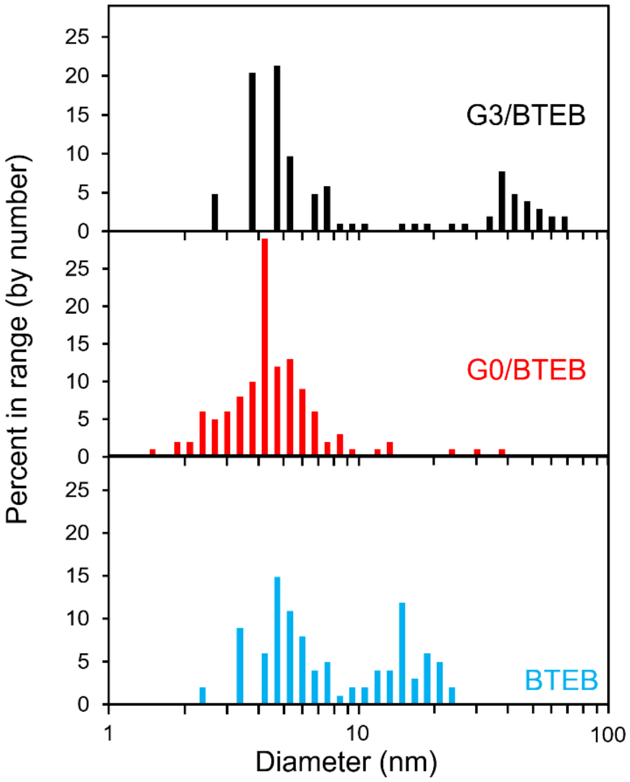

Figure 8 – Number-weighted size distribution of Au nanoparticles in pure BTEB, PAMAM-G0/BTEB and PAMAM-G3/BTEB gels

The SWAXS patterns of PAMAM-G0/BTEB, PAMAM-G3/BTEB and the pure BTEB gels impregnated with Au are illustrated in **Figure 9**, for $0.03 < q < 3$ Å^{-1}. The patterns are relatively featureless at $q <$ ~2.6 Å^{-1}. However, two well-defined peaks are observed at 2.70 and 2.72 Å^{-1} for both PAMAM systems (corresponding to pseudo-Bragg spacings of 2.33 and 2.31 Å, respectively), although no such features are evident in the Au-impregnated BTEB system. This suggests that the observed pseudo-Bragg peaks arise from two specific Au...S distances, with significantly less polydispersity evident in the case of the PAMAM-G3/BTEB system (based on the smaller full-widths at half-maximum (FWHM) observed). Previous studies have reported single-crystal XRD studies of well-defined Au(I)/thioformamide,[64] Au(I)/thiomalate[65] and thiolate/Au(0) clusters such as $[Au_{25}(SC_2H_4Ph)_{18}]$ and $[Au_{38}(SC_{12}H_{25})_{24}]$,[66-69] in which average Au-S distances of 2.283 to 2.386 Å were observed. Accordingly, it is tempting to assign the peaks observed in the SWAXS data in **Figure 9** to the $SiO_{1.5}$-R-S...Au bonds between the PAMAM matrix and the gold nanoparticles observed *via* TEM. However, the well-defined thiolate/Au clusters described above are highly ordered nanosystems, in which the thiolates are an integral component of the stable cluster structures. In contrast, the thiolate moieties in the PAMAM systems are immobilised on silsesquioxane matrices and interacting with the surfaces of polydisperse Au nanoparticle distributions with observed diameters of ~2 to > 20 nm (which, in many cases, are larger than the pores in the silsesquioxane matrices within which the thiol ligands are located). In addition, the size polydispersity of the Au nanoparticles is significantly higher in the case of the PAMAM-G3/BTEB system, in contrast to the sharper and more intense pseudo-Bragg peaks observed in the SWAXS data for this latter system. Hence, the pseudo-Bragg peaks observed at 2.31 and 2.33 Å are assigned to the presence of small Au clusters stabilised by thiolate ligands on the surface of the PAMAM pores, which are too small to be directly imaged by TEM under the conditions used in this study (and which are presumably smaller than the Au_{25} clusters in $[Au_{25}(SC_2H_4Ph)_{18}]$, which have dimensions of around 1.5 nm, excluding the thiolate ligands). The higher Au content in the Au-impregnated PAMAM-G3/BTEB system is thus assumed to be due to the presence of these clusters. In particular, the higher density of thiols on the surfaces of the pores in the PAMAM-G3/BTEB system would ensure that a larger number of the thiols would be correctly oriented to enable such thiolate-stabilised Au clusters to be formed, leading to less polydispersity in the ensemble of S-Au bond distances distributed around the peak values of 2.33 and 2.31 Å. Mechanistically, we speculate that growth of the Au nanoparticles observed *via* TEM in the gels occurs *via* coalescence of such small thiolate-stabilised Au clusters, with subsequent aging and growth of the Au nanoparticles occurring through diffusion of the clusters within the silsesquioxane pore network.

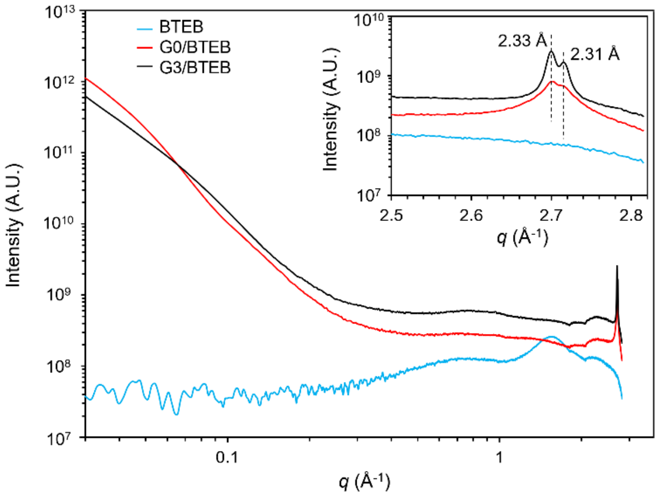

Figure 9 – SWAXS patterns of PAMAM-G0/BTEB (red), PAMAM-G3/BTEB (black) and pure BTEB gels (cyan) after impregnation with gold

2.2 PMO synthesis and inner dendrimer cleavage

The feasibility of developing more sophisticated PMOs, *via* templating with Pluronic P123, with dendrimers embedded in the walls was also investigated. It would be anticipated that the post-synthesis degradation of the inner part of the dendrimer (as demonstrated in **Section 2.1**) might enable PMOs with two types of pores to be created: one arising from templating of the SDA, and a second resulting from cleavage of the dendrimer with DTT. An additional objective was to generate functionalised pores within the walls of the PMO. The synthesis of such hierarchical structures was approached in three steps: synthesis of PMOs from the triethoxysilylated dendrimer in the presence of a structure directing agent (SDA); surfactant extraction; and finally, dendrimer cleavage. The approach is illustrated in **Figure 10**.

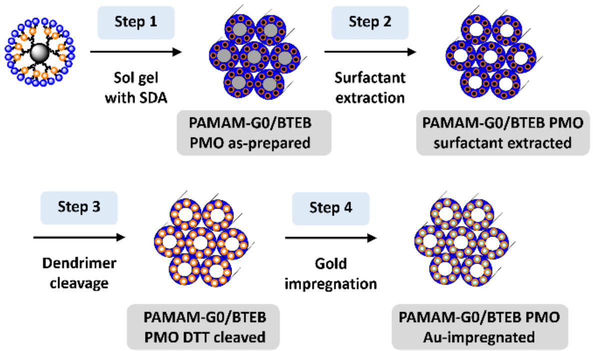

Figure 10 – Synthetic pathway to hierarchical PMOs with bimodal porosity and pendant functional groups

Here again, BTEB was used as a co-precursor with the PAMAM-Si(OEt)$_3$ dendrimer to consolidate the framework and promote organisation of the material during templating. Scoping studies with the PAMAM-G0 dendrimer system, which are described in **Section S3.3** (Supporting Information), were used to optimise the synthesis conditions, based on a protocol adapted from Inagaki.[70] It was necessary to increase the quantity of BTEB used in the synthesis to ensure that the dendrimer did not disrupt the organisation of the PMO (PAMAM-G0-Si(OEt)$_3$:BTEB = 1:384).

2.2.1 Chemical composition of PAMAM-G0/BTEB PMO. As expected, given the reduced concentration of dendrimer used, no features associated with the dendrimer could be observed by solid state NMR. FTIR spectra obtained at different steps during the synthesis, **Figure S21**, confirmed the presence of amide II and amide I bands at 1549 and 1632 cm^{-1}, respectively, as well as a peak at 1731 cm^{-1} in the PMO before and after surfactant extraction which is attributed to carbonyl moieties (**black** and **red** plots in **Figure S21**). This demonstrates that the dendrimer is retained in the silsesquioxane network during the first two steps of the PMO synthesis (**Figure 10**). The sharpness of the peaks observed in the FTIR spectrum of the PMO compared to the PAMAM gel suggests that the dendrimers are in a more ordered environment. In addition, the shift to lower wavenumber of the amide and C=O stretching bands suggests that the dendrimer has been partially cleaved at the ester bonds on the dendrimer backbone under the acidic conditions used during synthesis of the PMO but is still retained within the silsesquioxane network. In contrast, the loss of the amide II peak at 1549 cm^{-1} following DTT treatment (**Figure S21**) confirms the successful cleavage and quantitative removal of the dendrimer core. Presumably the enlarging of the pores accompanying cleavage of the disulfide linkage and associated removal of the HO-CH_2-CH_2-SH moieties that remained covalently bound to the silsesquioxane network following hydrolysis of the ester bond is sufficient to facilitate removal of the dendrimer core fragments by washing.

2.2.2 Textural properties of PAMAM-G0/BTEB PMO. The N_2 physisorption isotherms of the PAMAM-G0/BTEB PMO sample before surfactant extraction and after DTT treatment (**Figure 11(a)**; black and red curves, corresponding to PAMAM-G0/BTEB PMO "as-prepared" and "DTT cleaved" in **Figure 10**, respectively) exhibited similar type IV isotherms, demonstrating that the mesopore network remains intact following surfactant removal and dendrimer cleavage. The steep parallel branches on the adsorption and desorption arms at intermediate relative pressure is consistent with well-organised mesoporosity with monodisperse pore size. The BJH pore size distributions derived from the respective desorption branches (**Figure S22**) show a narrow pore size distribution centred around 6.3 nm for the sample before surfactant extraction and 5.7 nm after DTT cleavage of the dendrimer core (PAMAM-G0/BTEB PMO "as-prepared" and "DTT cleaved" in **Figure 10**, respectively). The decrease in the pore size is consistent with shrinkage of the pore network due to surfactant extraction, as is commonly observed. In addition, the horizontal saturation plateau observed above 550 cm^{3}.g^{-1} (**Figure 11(a)**) indicates that the material is mainly mesoporous. A more detailed analysis of the isotherms (**Table 3**) reveals that the small quantity of microporosity present in the samples is not impacted by DTT cleavage, indicating that no micropores are created by the dendrimer cleavage as observed in the case of the PAMAM-G0/BTEB gel. It would be anticipated that the removal of the surfactant and loss of the dendrimer core would lead to a small increase in the mesopore volume. However, a small decrease in both the mesopore volume and surface area are evident (**Table 3**), suggesting a loss of mesoporosity during cleavage. However, the key textural features are still retained.

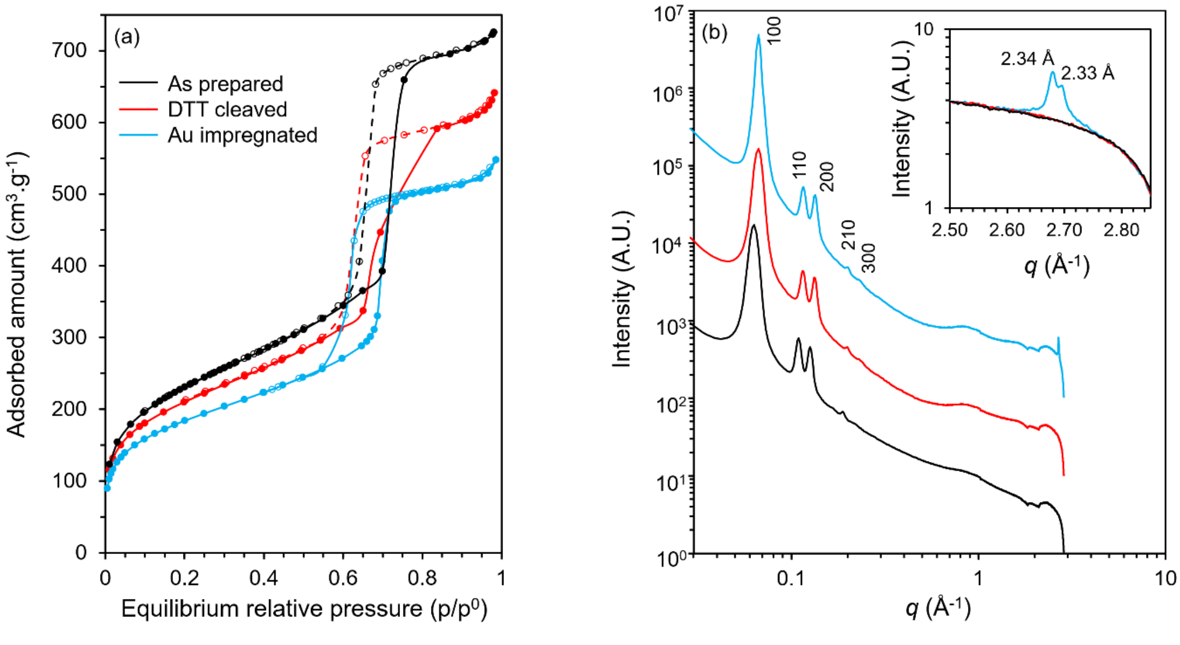

Figure 11 – N_2 physisorption isotherms (a) and SWAXS patterns (b) of the PAMAM-G0/BTEB PMO as-prepared (black); after DTT cleavage (red); and after Au impregnation (blue)

The SWAXS spectra (**Figure 11(b)**) for $q < 1.0$ Å^{-1} are consistent with the physisorption data and indicate a well-defined 2D-hexagonal mesostructure with a lattice parameter (pore diameter plus wall thickness) of 11.4 nm for the as-prepared PMO and 10.9 nm following subsequent DTT treatment (PMO DTT cleaved). The small decrease in periodicity observed after DTT treatment is consistent with the small decrease in mesoporosity and surface area observed *via* N_2 physisorption. The TEM micrograph of the PMO DTT cleaved sample (**Figure 12(a)**) is also consistent with a well-defined 2D-hexagonal network, with a spacing of around 10 nm being observed, consistent with the SWAXS data. The textural properties are summarised in **Table 3**.

Table 3 - Textural properties of PAMAM-G0/BTEB PMO prior to surfactant extraction (as-prepared); following surfactant extraction and DTT treatment (DTT cleaved); following Au impregnation (Au-impregnated) and of a pure BTEB PMO synthesised under the same conditions

Sample	BET SA* ($m^2.g^{-1}$)	Pore diameter (nm)	Wall thickness (nm)	Total PV** ($cm^3.g^{-1}$)	Micro PV ($cm^3.g^{-1}$)	Meso PV ($cm^3.g^{-1}$)
As-prepared	800	6.3	5.1	1.12	0.049	1.07
DTT cleaved	739	5.7	5.2	0.99	0.049	0.94
Au-impregnated	652	5.7	5.4	0.85	0.048	0.80
Pure BTEB as-prepared***	640	5.6	5.2	0.74	0.040	0.70

* SA : surface area, ** PV : pore volume, *** From Reference[71]

2.2.3 Impregnation with Au(III) salts and the formation of Au(0) nanoparticles. The formation of Au nanoparticles within the PAMAM-G0/BTEB PMO was investigated in a similar manner to that described for the gel samples (see **Section 2.1**). The N_2 physisorption isotherms and corresponding SWAXS patterns observed after Au impregnation (**Figure 11(b)**, blue plots) confirm the retention of the 2D-hexagonal mesoporous network following impregnation, with a decrease in surface area and mesopore volume due to Au nanoparticles retained within the pores (**Table 3**). In addition to the expected features associated with the 2D-hexagonal PMO structure, the SWAXS pattern of the sample obtained after Au impregnation exhibits additional peaks near 2.7 Å^{-1} which are not observed in the samples obtained after surfactant removal or DTT cleavage. These features are attributed to thiolate/Au clusters[64-68] similar to those observed in the PAMAM-G0/BTEB and PAMAM-G3/BTEB gels, which are presumably the precursor species leading to the formation of the Au nanoparticles.

The corresponding TEM micrograph, **Figure 12(b),** reveals the formation of a small number of well-defined, monodisperse Au nanoparticles following impregnation, with the size of the nanoparticles being comparable to that of the mesopores (5-6 nm). These observations suggest that in the PAMAM-G0/BTEB PMO system, formation of the Au nanoparticles is confined to the uniform mesopore channels, with a single nucleation event and controlled growth leading to monosized nanoparticles due to the lower number of surface thiols (lower PAMAM:BTEB ratio), correspondingly lower concentration of Au species and pore size restriction. In contrast, the higher surface thiol (and Au content) in the PAMAM-G0/BTEB gel system promotes secondary nucleation, coalescence, and growth processes, leading to a polydisperse Au nanoparticle size distribution (which includes the presence of nanoparticles that are significantly larger than the pores), with growth of the Au nanoparticles occurring both within the pore network and on the external surface of the gel network.

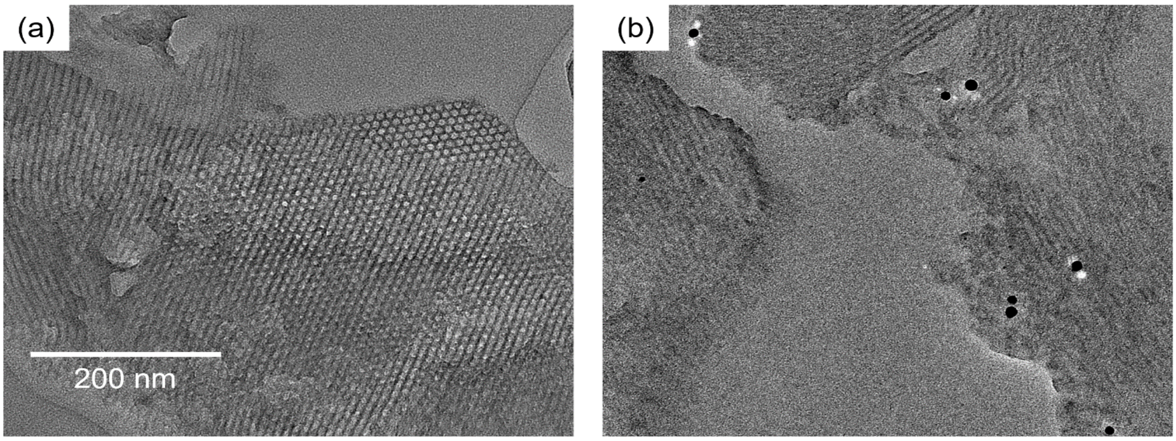

Figure 12 – TEM micrographs of PAMAM-G0/BTEB PMO following DTT treatment (a) and Au impregnation (b)

Previous studies of the formation of Au nanoparticles in mesoporous silica functionalised with thiol by either co-condensation[72] or post grafting[73] have clearly observed Au nanoparticles with dimensions of around 1.5-2 nm in the PMO channels *via* TEM. Corriu's group described a PMO system[74] in which thiol groups were formed within the pore walls by cleavage of a disulfide-bridged bistriethoxysilane compound, followed by subsequent impregnation with Au salts to produce Au nanoparticles localised within the walls. In this latter case, TEM images of the ~2 nm Au nanoparticles exhibited low image contrast, although their presence within the walls was inferred by a decrease in the micropore volume and an increase in the X-ray scattering contrast between the pore walls and channels after impregnation. The corresponding X-ray diffraction patterns did not reveal any evidence for the formation of uniform thiolate/Au clusters. In contrast, in our system, the presence of diffraction peaks arising from $SiO_{1.5}$-R-S…Au moieties unequivocally confirm the formation of uniform Au nanocluster in the cavity generated by the removal of the inner part of the dendrimer and subsequent thiol formation. The TEM image contrast does not enable the unambiguous localisation of the Au cluster due to their small size.

However, a small, but distinct, increase in the intensity of the (100), (110) and (200) pseudo-Bragg peaks (see **Figure S23**) is attributed to an increase of the electronic contrast between the pore walls and pore channels after Au impregnation, thus suggesting that the Au nanoclusters are localised in cavities within the walls of the PMO (note that the X-ray scattering length densities of Au^0; a representative Au/thiol cluster, $(Au_{38}(SC_2H_4Ph)_{24}$; silylated PAMAM after sol-gel processing and core cleavage; hydrolysed and condensed BTEB, $(SiO_{1.5})_2C_6H_4$; and H_2O are 131, 24.7, 15.4, 15.2, and 9.4 x 10^{10} cm^{-2}, respectively). A more detailed analysis of the textural properties of the PAMAM G0/BTEB PMO before and after Au impregnation provides additional evidence for the presence of the observed 5-6 nm Au nanoparticles within the 2D-hexagonal mesopore network. The data in **Table 3** indicate that Au impregnation is accompanied by two key changes in the textural properties, namely (a) a decrease in specific surface area (by around 12 % on a "per-gram" basis); and (b) a decrease in the mesopore volume (by around 15 % on a "per-gram" basis). Part of this decrease can be attributed to an increase in the mass of the sample following Au impregnation. The fractional decrease is greater in the case of the specific mesopore volume, suggesting that some of the mesoporosity is blocked following impregnation. However, it is noteworthy that the diameter of the mesopores does not decrease following impregnation. Consequently, we conclude that the mesopores are partially blocked by the 5-6 nm Au nanoparticles observed *via* TEM, consistent with the Au nanoparticles being confined within the mesopore network and hence contributing to the observed decrease in pore volume without a corresponding decrease in pore diameter.

1. Conclusions

A multifunctional PAMAM-based dendrimer has been synthesised by grafting a tailor-made cleavable linker onto the arms of commercially available PAMAM dendrimers (generations zero and three), followed by the introduction of a condensable triethoxysilyl group on the dendrimers' periphery *via* a CuAAc click reaction. The disulfide group was chosen as a cleavable site due to its capacity to be cleaved under chemical or enzymatic conditions (and to generate thiol functions localised within the pores), while the silane was chosen for its capacity to generate an extended silsesquioxane network *via* sol-gel processing.

The multifunctional dendrimers were subsequently employed in a sol-gel process, either alone or in combination with BTEB, to obtain silsesquioxane gels with dendrimers covalently embedded within the interior of the organosilica network. Chemical cleavage of the disulfide bond by treatment with dithiothreitol, and subsequent removal of the dendrimer core by washing, resulted in the formation of porous organosilicas with thiol functions located within the pores. The effect of different dendrimer generations (G0 or G3) on the reactivity of the pendant thiol functions was probed by impregnation with gold salts, which were reduced to obtain gold nanoparticles within the pore networks of the gels and PMO. The gels yielded polydisperse gold nanoparticles (2 to 70 nm) with dimensions modulated by the generation of the dendrimer, together with well-defined gold/thiolate clusters with Au…S distances of 2.3 Å. Such clusters were also observed in the PMO system, together with monodispersed gold nanoparticles with diameters comparable to that of the organised pores in the PMO. The presence of organised porosity together with a lower density of surface thiol species in the latter system promotes the formation of monodisperse nanoparticles, avoiding the multiple nucleation events leading to a polydisperse size distribution in the case of the gels. Moreover, no SWAXS peaks near d=2.3 Å were observed in the case of pure BTEB gel impregnated with gold, as expected from the absence of thiol functions in the latter system to complex the gold salts.

A range of potential applications can be envisaged for such multifunctional materials, including environmental remediation (*e.g.*, removal of heavy metals such as mercury), catalysis (including multi-site catalysis for cascade reactions), sensing and optics (in particular through the size-controlled synthesis of gold nanoparticles). The PAMAM core could also be used as a carrier for drug delivery applications, due to the possibility of releasing the inner part of the dendrimer under biological conditions by enzymatical cleavage. Although not demonstrated in our work, we note the possibility of recovering the inner part of the dendrimer for subsequent reuse in the synthesis of new dendrimers *via* a thiol disulfide exchange reaction, highlighting a significant economic advantage of the method in the case of (expensive) high generation dendrimers.

2. Experimental

4.1 Chemicals

Hydroxyethyl-(propargyloxyethyl)disulfide was synthesised as previously described[75] and purified by successive flash column chromatography steps, with an increasing gradient of dichloromethane (DCM)/ethyl acetate followed by cyclohexane/ethyl acetate. PAMAM-G0 dendrimer was prepared[76] from distilled ethylenediamine and methylacrylate (Alfa Aesar). Bis-(triethoxysilylpropyl)amine azidoethane was synthesised using a procedure previously described by our group.[52] Similarly, BTEB was prepared following previously reported protocols[62, 77] and purified by distillation under vacuum.

Acryloyl chloride (Alfa), PAMAM-G3 dendrimer (Sigma Aldrich, 20% in MeOH), tetrabutylammonium fluoride (TBAF, Sigma Aldrich, 1 M solution in tetrahydrofuran (THF)), Pluronic P123 (Sigma Aldrich), DTT (Alfa Aesar, 98%), sodium gold tetrachloride ($NaAuCl_4$, Sigma Aldrich, 99%) and sodium borohydride ($NaBH_4$, Sigma Aldrich, 99.99%) were used as received (see **Section S2.4** in the Supporting Information for details of gold impregnation experiments). Copper iodide (Sigma Aldrich, 99.999%) was dried with P_2O_5 prior to use. Triethylamine (Alfa Aesar) and diisopropylethylamine (TCI) were distilled over NaOH. Dry methanol was purchased from Acros (Acroseal®) and used as received. THF, chloroform, DCM, cyclohexane, ethyl acetate, methanol, water (HPLC grade), ethanol (absolute grade), acetone (Normapur) and hydrochloric acid solution (35 %) were obtained from VWR and used as received unless indicated otherwise.

4.2 Preparation of the functionalised dendrimers

4.2.1 Synthesis of (propargyloxyethyl)(ethylacrylate)disulfide linker. In a flame-dried Schlenk flask, a solution of hydroxyethyl-(propargyloxyethyl)disulfide (19.8 mmol, 3.8 g, 1 eq) in dry chloroform (31 mL) was prepared under an inert atmosphere. Distilled triethylamine (59.4 mmol, 8.0 mL, 3 eq) was added to the solution to sequester HCl. The solution was placed in an ice bath and the Schlenk flask was purged with nitrogen for 15 min. Acryloyl chloride (29.7 mmol, 2.4 mL, 1.5 eq) was then added dropwise. The injection was followed by the appearance of precipitated salts and an orange coloration. After 24 h at 25 °C, the reaction mixture was filtered over celite® and the solvent was evaporated. The crude reaction product was purified on a silica pad eluted with a 90/10 mixture of cyclohexane/ethyl acetate. The solvents were evaporated under reduced pressure and the product was recovered as a colourless oil. **Yield:** 77% ($C_{10}H_{14}O_3S_2$, 3.76 g, 15.3 mmol) **^{1}H NMR (400 MHz, CDCl$_3$, δ, ppm):** 6.44 (dd, 1H, J_1=17.4 Hz, J_2=1.4 Hz, **CH$_2$**=CH-(C=O)), 6.13 (dd, 1H, J_1=17.4 Hz, J_2=10.4 Hz, CH$_2$=**CH**-(C=O)), 5.86 (dd, 1H, J_1=10.4 Hz, J_2=1.4 Hz, **CH$_2$**=CH-(C=O)), 4.43 (t, 2H, J=6.6 Hz, S-CH$_2$-**CH$_2$**-O-(C=O)), 4.19 (d, 2H, J=2.4 Hz, HC≡C-**CH$_2$**-O), 3.79 (t, 2H, J=6.4 Hz, CH$_2$-O-**CH$_2$**-CH$_2$-S), 2.98 (t, 2H, J=6.6 Hz, S-**CH$_2$**-CH$_2$-O-(C=O)), 2.93 (t, 2H, J=6.4 Hz, CH$_2$-O-CH$_2$-**CH$_2$**-S), 2.46 (t, 1H, J=2.4 Hz, **HC**≡C-CH$_2$-O) **^{13}C NMR (100 MHz, CDCl$_3$, δ, ppm):** 165.98 (C=O), 131.36 (**CH$_2$**=CH), 128.17 (CH$_2$=**CH**), 79.40 (CH≡**C**), 74.89 (**CH**≡C), 68.10 (S-CH$_2$-**CH$_2$**-O$_{\text{Acetylenic}}$), 62.55 (S-CH$_2$-**CH$_2$**-O$_{\text{Acrylate}}$), 58.28 (CH≡C-**CH$_2$**-O), 38.64 and 37.30 (S-**CH$_2$**-CH$_2$-O$_{\text{Acetylenic}}$ and S-**CH$_2$**-CH$_2$-O$_{\text{Acrylate}}$) **IR (ν, cm^{-1}):** 3287 (≡C-H), 1724 (C=O), 668 (C-S) **HR ESI-MAS (M+Na):** obtained 269.0 m/z, expected 269.04 m/z.

4.2.2 General route to acetylenic PAMAM dendrimers. In a flame-dried Schlenk flask, a solution of (propargyloxyethyl)-(ethylacrylate)disulfide (2 eq/NH) in dry methanol was prepared under an inert atmosphere. The solution was placed in an ice bath. A solution of PAMAM-(NH$_2$)$_n$ (1 eq, where n = 4 or 32 for G0 and G3, respectively) in dry methanol was added dropwise at 0 °C. The syringe was washed with dry methanol and the reacting mixture was returned to room temperature. After 3 days of reaction at 25 °C, the solvent was evaporated. The subsequent purification step, which yielded a yellow oil, was dependent on the dendrimer generation as described below for the G0 and in the Supporting Information (**Section S2.1**) for the G3 dendrimer.

PAMAM-G0 S-S propargyl dendrimer: The reaction was performed with (propargyloxyethyl)(ethylacrylate)disulfide (8.0 mmol, 2.0 g, 2 eq/NH) in dry methanol (0.4 mL) and PAMAM-G0-(NH$_2$)$_4$ (0.5 mmol, 247 mg, 1 eq) in dry methanol (1.5 mL). The crude reaction product was purified using a neutral alumina pad eluted with an 80/20 mixture of cyclohexane/ethyl acetate. The product was recovered after elution with a 95/5 mixture of ethyl acetate/methanol. A yellow oil was obtained and dried under vacuum. **Yield:** 63% ($C_{102}H_{160}N_{10}O_{28}S_{16}$, 788 mg, 0.3 mmol) **^{1}H NMR (400 MHz, CDCl$_3$, δ, ppm):** 4.34 (t, 16H, J=6.6 Hz, S-CH$_2$-**CH$_2$**-O-(C=O)) 4.20 (d, 16H, J=2.4 Hz, HC≡C-**CH$_2$**-O), 3.79 (t, 16H, J=6.4 Hz, CH$_2$-O-**CH$_2$**-CH$_2$-S), 3.67 (s, 4H, **PAMAM core**), 3.26 (m, 8H, **PAMAM branch**), 2.93 (m, 32H, S-**CH$_2$**-CH$_2$-O-(C=O) & CH$_2$-O-CH$_2$-**CH$_2$**-S), 2.80 (m, 24H, **PAMAM branch** & N-CH$_2$-**CH$_2$**-(C=O)), 2.50 (m, 36H, **PAMAM branches** & N-**CH$_2$**-CH$_2$-(C=O) & **HC**≡C-CH$_2$-O), 2.34 (t, 8H, J=5.6 Hz, **PAMAM branch**) **^{13}C NMR (100 MHz, CDCl$_3$, δ, ppm):** 172.48, 172.40, 79.48, 75.04, 68.19, 62.53, 60.32, 58.28, 52.94, 49.26, 41.49, 38.56, 38.43, 37.22, 32.70. **IR (ν, cm^{-1}):** 3287 (≡C-H), 1732 (C=O), 1649 (amide I), 1534 (amide II) **MALDI-MS:** obtained 2486.8 m/z, expected (M+2H)$^+$, 2486.7 m/z.

4.2.3 General procedure for obtaining triethoxysilylated dendrimers via click reactions. In a flame-dried microwave tube, a solution of dry CuI (5 mol%) and distilled diisopropylethylamine (DIPEA, 2 eq/alkyne) in dry DCM was added, under an inert atmosphere, to a solution of dendrimer (R-C≡CH)$_n$ (1 eq) in dry DCM. Then a solution of bis-(triethoxysilylpropyl)aminoethenylazide (1 eq/alkyne) in dry DCM was injected into the reaction mixture. The mixture was stirred under microwave irradiation at 60 °C (200 W). The completion of the reaction was verified by ^{1}H NMR spectroscopy and the solvent was evaporated under reduced pressure. The subsequent synthesis of the G0 dendrimer is described in detail below, while that of the G3 dendrimer is described in the Supporting Information (**Section S2.2**)

*PAMAM-G0 S-S triethoxysilane dendrimer***:** The reaction was performed with PAMAM-G0 S-S (R-C≡CH)$_8$ (60.3 µmol, 150 mg) in dry DCM (3.3 mL), bis-(triethoxysilylpropyl) aminoethenylazide (496 µmol, 241 mg, 1 eq/alkyne) in dry DCM (3.3 mL) and a solution of dry CuI (24.1 µmol, 4.9 mg, 5 mol%) and distilled DIPEA (965 µmol, 170 µL, 2 eq/alkyne) in dry DCM (3.3 mL). The reaction was held for 20 min under microwave irradiation at 60 °C. The product was obtained as a yellow-green oil. **Yield:** quantitative ($C_{262}H_{528}N_{42}O_{76}S_{16}Si_{16}$, 388.6 mg, 60.2 µmol) **^{1}H NMR (400 MHz, CDCl$_3$, δ, ppm):** 7.67 (s, 8H, **H$_{\text{triazole}}$**), 4.63 (s, 16H, O-**CH$_2$**-C$_{\text{triazole}}$), 4.35 (t, 16H, J=6.3 Hz, N$_{\text{triazole}}$-**CH$_2$**-CH$_2$-N), 3.78 (m, 128H, CH$_2$-O-**CH$_2$**-CH$_2$-S & O-**CH$_2$**-CH$_3$ & S-CH$_2$-**CH$_2$**-O-(C=O)), 3.51 (s, 4H, **PAMAM core**), 3.24 (m, 8H, **PAMAM branch**), 2.86 (m, 48H, S-**CH$_2$**-CH$_2$-O-(C=O) & CH$_2$-O-CH$_2$-**CH$_2$**-S & N$_{\text{triazole}}$-CH$_2$-**CH$_2$**-N), 2.73 (t, 16H, J=6.6 Hz, N-CH$_2$-**CH$_2$**-(C=O)), 2.51 (t, 8H, J=6.1 Hz, **PAMAM branch**), 2.43 (m, 56H, **PAMAM branch** & N-**CH$_2$**-CH$_2$-(C=O) & N-**CH$_2$**-CH$_2$-CH$_2$-Si), 2.33 (t, 8H, J=5.6 Hz, **PAMAM branch**), 1.45 (quin, 32H, J=7.4 Hz, CH$_2$-**CH$_2$**-

CH_2-Si), 1.19 (t, 144H, J=7.1 Hz, CH_3-**CH_2**-O-Si), 0.51 (t, 32H, J=7.4 Hz, CH_2-CH_2-**CH_2**-Si) **^{13}C NMR (100 MHz, $CDCl_3$, δ, ppm):** 173.00, 172.90, 144.21 (triazole), 123.51 (triazole), 68.35, 64.11, 60.31, 58.37 (ethoxy), 57.07, 54.18, 49.29, 48.94, 41.24, 38.62, 37.18, 33.84, 32.69, 20.33, 18.31 (ethoxy), 7.82 **^{29}Si NMR (80 MHz, $CDCl_3$, δ, ppm):** -45.20 **IR (ν, cm^{-1}):** 1736 (C=O), 1654 (amide I), 1554 (amide II), 1077 (C-O_{ethoxy}) **MALDI-MAS:** An appropriate desorption matrix could not be identified.

4.3 Preparation of gels

The synthesis of gels from the G0 dendrimer, and their subsequent treatment with DTT to cleave the disulfide bond is described in detail below, while details of the synthesis of the corresponding G3 materials is included in the Supporting Information (**Section S2.3**).

4.3.1 Synthesis of PAMAM-G0 gel and DTT treatment. In a flame-dried Schlenk flask, the solution of PAMAM-G0-Si$(OEt)_3$ (119 µmol, 763 mg, 1 eq) resulting from the click reaction described above was dried under vacuum. The resulting PAMAM-G0-Si$(OEt)_3$ viscous oil was then re-dissolved in dry THF (1.3 mL) under nitrogen. Water (1.9 mmol, 34 µL, 1 eq/Si) was added followed by TBAF solution (1 M in THF, 38 µmol TBAF, 38 µL solution, 0.02 eq/Si). The mixture formed a gel within a few minutes. The material was then aged for 3 days. After aging, the dark green solid was divided into two parts. One third of the solid was crushed, washed three time with water and three times with acetone then dried under vacuum overnight to yield a green powder. **^{13}C NMR (75 MHz, CP-MAS, δ, ppm):** 144.3 (triazole), 124.0 (triazole), 52.2-10.6 (cluster) **^{29}Si NMR (60 MHz, CP-MAS, δ, ppm):** -58.3 (T^2_{PAMAM}), -66.1 (T^3_{PAMAM}) **IR (ν, cm^{-1}):** 1736 (C=O), 1653 (amide I), 1548 (amide II), 1142-1013 (Si-O-Si).

The remaining two thirds were suspended in water (10 mL). In order to outgas the solvent, five freeze/pump/thaw cycles were performed. An excess of DTT (1.89 mmol, 290 mg, 2 eq/max quantity of S-S) was then added under an inert atmosphere to cleave the disulfide bonds. The reaction was stirred at room temperature for three days. After cleavage, the solid was washed three times with water, three times with acetone and dried under vacuum overnight. **^{13}C NMR (75 MHz, CP-MAS, δ, ppm):** 144.0 (triazole), 124.0 (triazole), 54.6-11.8 (cluster) **^{29}Si NMR (60 MHz, CP-MAS, δ, ppm):** -65.8 (T^3_{PAMAM}) **IR (ν, cm^{-1}):** 1736 (C=O), 1142-1013 (Si-O-Si).

4.3.2 Synthesis of PAMAM-G0/BTEB gel and DTT treatment. In a flame-dried Schlenk flask, the solution of PAMAM-G0-Si$(OEt)_3$ (40.3 µmol, 260 mg, 1 eq) resulting from the click reaction was mixed with BTEB (1.9 mmol, 780 µL, 48 eq). The mixture was dried under vacuum to obtain a PAMAM-G0-Si$(OEt)_3$ solution in BTEB. The mixture was dissolved in dry THF (3.0 mL) under nitrogen. Water (4.5 mmol, 81 µL, 1 eq/Si) was added, followed by TBAF (1 M in THF, 90.3 µmol TBAF, 90 µL solution, 0.02 eq/Si). The mixture formed a gel within a few minutes. The material was then aged for 3 days. After aging, the green solid was crushed, washed three times with water and three times with acetone then dried under vacuum overnight to obtain a green powder. **^{13}C NMR (75 MHz, CP-MAS, δ, ppm):** 133.7 (aromatic BTEB), 58.8 (residual ethoxy), 17.9 (residual ethoxy) **^{29}Si NMR (60 MHz, CP-MAS, δ, ppm):** -53.7 (T^1_{PAMAM}), -66.6 (T^3_{PAMAM}), -72.9 (T^2_{BTEB}) **IR (ν, cm^{-1}):** 1737 (C=O), 1660 (amide I), 1153-1020 (Si-O-Si).

A portion of the PAMAM-G0/BTEB gel (400 mg) was added to water (10 mL), which was outgassed by five freeze/pump/thaw cycles prior to the addition. DTT (350 µmol, 54 mg, 1.5 eq/expected quantity of S-S) was then added under an inert atmosphere to cleave the disulfide bonds. The reaction was stirred at room temperature for five days. After cleavage, the solid was washed three times with water, three times with acetone and dried under vacuum overnight. **^{13}C NMR (75 MHz, CP-MAS, δ, ppm):** 133.4 (aromatic BTEB), 58.9 (residual ethoxy), 17.4 (residual ethoxy) **^{29}Si NMR (60 MHz, CP-MAS, δ, ppm):** -61.1 (T^1_{BTEB}), -70.5 (T^2_{BTEB}), -78.1 (T^3_{BTEB}) **IR (ν, cm^{-1}):** 1153-1020 (Si-O-Si).

4.4 Preparation of PAMAM G0/BTEB PMO

In a flame dry Schlenk flask, a solution of PAMAM-G0-Si$(OEt)_3$ (3.6 µmol, 23.2 mg) was evaporated together with BTEB (1.4 mmol, 562 mg, 384 eq). The mixture was dried overnight under reduced pressure. The remaining solvent was then further evacuated by five freeze/pump/thaw cycles. In a Schlenk vessel, Pluronic P123 (96.5 µmol, 563 mg, 0.034 eq/Si) was dissolved at 35 °C in water (20.5 mL) under strong agitation (1400 rpm). After complete dissolution of P123, HCl 35% (1.2 µmol HCl, 127 µL, $0.4x10^{-3}$ eq/Si) was added to the surfactant solution and the resulting mixture was then cooled to 0 °C. The 1/384 dendrimer/BTEB silane mixture (585 mg) was added dropwise to the cold solution. After 1 h of reaction, the reacting mixture was heated to 35°C for 24 h and then to 100 °C for an additional 24 h. The white solid obtained was recovered by centrifugation, washed with water until the pH of the supernatant reached 6.5 and then returned to the vessel in 20.5 mL of water at 100 °C for further aging and structural consolidation for three days. The resulting solid was then recovered by centrifugation, washed once with water, twice in ethanol, once in acetone and dried under vacuum to afford a white powder (296 mg).

The surfactant extracted material was obtained by stirring the previously synthesised PMO (212 mg) in an acidic solution of ethanol (4.3 mL of HCl 35% in 142 mL ethanol) at 85 °C for 4.5 days. The dispersion was then centrifuged, and the resulting solid was washed with water until the pH value of the supernatant reached 6.5 and with acetone three times. The material was finally dried under vacuum to obtain a white powder (174 mg).

The surfactant-free PMO (174 mg) was dispersed in outgassed water (5 mL) under inert atmosphere. DTT (81.6 µmol, 12.6 mg, 1.5 eq./max quantity of S-S) was added and the mixture was stirred for 4.5 days at room temperature. The resulting solid was separated, washed three times with water then acetone and dried under reduced pressure to obtain a white powder (123 mg).

4.5 Methods and characterisation

Liquid ^{1}H, ^{13}C and ^{29}Si NMR spectra were obtained at 25 °C on a Bruker Avance 400 MHz spectrometer in $CDCl_3$ and at concentrations of around 10 mg/mL. ^{29}Si and ^{13}C spectra were proton decoupled. ^{29}Si and ^{13}C solid-state NMR spectra were recorded using cross-polarisation and magic-angle spinning techniques (CP-MAS) on a Bruker DSX 300 MHz spectrometer. High resolution TOF-ESI and MALDI mass spectra were acquired using a Waters Synapt G2-S and Bruker RapifleX spectrometer (with dithranol/sodium trifluoroacetate as desorption matrix), respectively.

Mid-infrared spectra (MIR: 4000–400 cm^{-1}) of liquid samples were obtained at room temperature using a Bruker Tensor 27 spectrometer equipped with a KBr beam splitter, a Black body source, a DLATGS detector and an attenuated total reflectance (ATR) accessory (diamond waveguide). MIR spectra of the pure PAMAM-G0 gel and PAMAM- G0/BTEB gels were recorded in transmission using a Bruker IFS66 vacuum spectrometer equipped with a KBr beam splitter, a Black body source and a DTGS detector. KBr pellets were prepared with 1.2 mg of sample and 300 mg of KBr and were dried at 65 °C for 24-72 hours to remove water absorbed in the KBr. Higher temperatures were not used, due to the potential risk of damaging the dendrimer skeleton. The wavelength dependency of the penetration depth into the sample and the anomalous dispersion of the IR beam result in some systematic differences between spectra measured using the ATR and the transmission-technique. To obtain a better comparability of ATR and transmission spectra, the ATR spectra were corrected using the classical "Extended ATR correction" function provided by the OPUS (Bruker optics Inc.) software. Due to the spectral cutoff of the diamond in the ATR accessories, data between 2100 and 2600 cm^{-1} were set to zero. Raman spectroscopy was performed using a Renishaw inVia^{TM} Raman microscope system. The neat powders were analysed at a magnification of x50, using 785 nm laser excitation and an exposure time of 100 s for the materials and dithiothreitol. A 20 s exposure time was used in the case of the bis(hydroxysilyl)disulfide, to avoid saturation from the luminescent background generated during exposure to the 785 nm excitation. As the measurements were impacted by luminescence, a baseline correction treatment was performed.

Transmission electron microscopy (TEM) images of the samples before gold impregnation were obtained using a JEOL 1400 P+ microscope operating at 120 kV with a LaB_6 source. After gold impregnation, samples were analysed on a JEOL 2200FS – 200 kV apparatus, equipped with an EDX– SDD Oxford Instrument XMaxN 100 TLE detector. All samples were prepared by microtome with a nominal thickness of around 70 nm, with the exception of gold-impregnated samples which were prepared by simple deposition on a copper grid coated with carbon film.

Nitrogen physisorption isotherms were obtained using a Micromeritics ASAP 2020 machine at 77.35 K and with samples activated at 80 °C for 12 h under secondary vacuum. The specific surface area of the materials was determined using the BET model in the relative pressure range $0.05 < p/p° < 0.25$. The pore size distributions were derived using the BJH model, applied on the desorption branches. The mesopores volumes were further derived from the relative pressure at which saturation of the mesoporosity occurs ($p/p° = 0.85$). The occurrence of microporosity was evaluated using the t-plot method, taking the Harkins Jura equation as reference sorption isotherm.

Small- and wide-angle X-ray scattering (SWAXS) data were obtained using a Guinier-Mering set-up coupled with a 2D image plate detector. The X-ray source was a molybdenum anode ($\lambda = 0.71$ Å, E = 17.4 keV) providing structural information over scattering vector, q, ranging from 0.02 to 2.5 Å^{-1}. The experimental resolution was $\Delta q/q = 0.05$. The region between the sample and the image plate was purged with flowing helium, to avoid air absorption. The image azimuthal average was determined using FIT2D software from ESRF (France), and data corrections and radial averaging were performed *via* standard procedures. X-ray scattering length densities of the BTEB matrix, silylated PAMAM dendrimer, Au and Au clusters were calculated from the stoichiometries, formula weights and densities of the respective materials using standard procedures. Where the densities were not available, van der Waal molecular volumes were calculated using the approaches reported by Bondi[78] and Zhao *et al.*[79]

The size distribution of the gold nanoparticles in each sample was determined by manual measurement using Adobe Photoshop software, with 100-200 nanoparticles used for each analysis. The results are presented as number-weighted distributions.

Conflicts of interest

There are no conflicts to declare.

Acknowledgements

The authors are thankful to Philippe Gaveau and Emmanuel Fernandez (Laboratoire de Mesures Physiques, Université de Montpellier, Ecole Nationale Supérieure de Chimie de Montpellier) for solid-state NMR experiments as well as David Maurin (Université de Montpellier, L2C) for his support in the FTIR experimental measurements. Access to the IR-Raman Technological Platform of the Université de Montpellier for undertaking the Raman experiments is gratefully acknowledged. The French Ministère de l'Enseignement Supérieur et de la Recherche is also acknowledged for the PhD scholarship of ML. NH thanks the University of Heidelberg and the ENSCM for financial support for an ERASMUS Exchange Internship.

Notes and references

1. M. Sowinska and Z. Urbanczyk-Lipkowska, *New J. Chem.*, 2014, **38**, 2168-2203.
2. A. W. Bosman, H. M. Janssen and E. W. Meijer, *Chem. Rev.*, 1999, **99**, 1665-1688.
3. E. Buhleier, W. Wehner and F. Vögtle, *Synthesis*, 1978, **1978**, 155-158.
4. D. A. Tomalia, H. Baker, J. Dewald, M. Hall, G. Kallos, S. Martin, J. Roeck, J. Ryder and P. Smith, *Polym J*, 1985, **17**, 117-132.
5. D. A. Tomalia, H. Baker, M. Hall, G. Kallos, S. Martin, J. Ryder and P. Smith, *Macromolecules*, 1986, **19**, 2466-2468.
6. A. M. Caminade and J. P. Majoral, *Molecules*, 2018, **23**.
7. C. Wörner and R. Mülhaupt, *Angew. Chem. Int. Ed. Engl.*, 1993, **32**, 1306-1308.
8. E. M. M. de Brabander-van den Berg and E. W. Meijer, *Angew. Chem. Int. Ed. Engl.*, 1993, **32**, 1308-1311.
9. L. L. Zhou and J. Roovers, *Macromolecules*, 1993, **26**, 963-968.
10. N. Launay, A. M. Caminade, R. Lahana and J. P. Majoral, *Angew. Chem. Int. Ed. Engl.*, 1994, **33**, 1589-1592.
11. D. A. Tomalia, *New J. Chem.*, 2012, **36**, 264-281.
12. C. Valerio, J. L. Fillaut, J. Ruiz, J. Guittard, J. C. Blais and D. Astruc, *J. Am. Chem. Soc.*, 1997, **119**, 2588-2589.
13. A. W. Kleij, R. A. Gossage, R. J. M. Klein Gebbink, N. Brinkmann, E. J. Reijerse, U. Kragl, M. Lutz, A. L. Spek and G. Van Koten, *J. Am. Chem. Soc.*, 2000, **122**, 12112-12124.
14. Z. Zhou, M. Cong, M. Li, A. Tintaru, J. Li, J. Yao, Y. Xia and L. Peng, *Chem. Commun.*, 2018, **54**, 5956-5959.
15. S. M. Grayson and J. M. J. Fréchet, *Chem. Rev.*, 2001, **101**, 3819-3867.
16. D. Astruc, E. Boisselier and C. Ornelas, *Chem. Rev.*, 2010, **110**, 1857-1959.
17. S. H. Medina and M. E. H. El-Sayed, *Chem. Rev.*, 2009, **109**, 3141-3157.
18. A. P. Dias, S. da Silva Santos, J. V. da Silva, R. Parise-Filho, E. Igne Ferreira, O. E. Seoud and J. Giarolla, *Int. J. Pharm.*, 2020, **573**.
19. A. K. Mandal, *Int. J. Polym. Mater. Polym. Biomater.*, 2021, **70**, 287-297.
20. S. Svenson and D. A. Tomalia, *Adv. Drug Deliv. Rev.*, 2005, **57**, 2106-2129.
21. C. C. Lee, J. A. MacKay, J. M. J. Frechet and F. C. Szoka, *Nat. Biotechnol.*, 2005, **23**, 1517-1526.
22. A. M. Caminade and J. P. Majoral, *Dalton Trans.*, 2019, **48**, 7483-7493.
23. R. M. Crooks, M. Zhao, L. Sun, V. Chechik and L. K. Yeung, *Acc. Chem. Res.*, 2001, **34**, 181-190.
24. A. K. Ilunga and R. Meijboom, *Catal Lett*, 2019, **149**, 84-99.
25. K. Yamamoto, T. Imaoka, M. Tanabe and T. Kambe, *Chem. Rev.*, 2020, **120**, 1397-1437.
26. S. M. Fatemi, S. J. Fatemi and Z. Abbasi, *Polym. Bull.*, 2020, **77**, 6671-6691.
27. R. Esfand and D. A. Tomalia, *Drug Discov. Today*, 2001, **6**, 427-436.
28. A. El Kadib, N. Katir, M. Bousmina and J. P. Majoral, *New J. Chem.*, 2012, **36**, 241-255.
29. G. J. A. A. Soler-Illia and O. Azzaroni, *Chem. Soc. Rev.*, 2011, **40**, 1107-1150.
30. I. Díaz, B. García, B. Alonso, C. M. Casado, M. Morán, J. Losada and J. Pérez-Pariente, *Chem. Mater.*, 2003, **15**, 1073-1079.
31. P. Reinert, J. Y. Chane-Ching, L. Bull, R. Dagiral, P. Batail, R. Laurent, A. M. Caminade and J. P. Majoral, *New J. Chem.*, 2007, **31**, 1259-1263.
32. R. Taheri, N. Bahramifar, M. R. Zarghami, H. Javadian and Z. Mehraban, *Powder Technol.*, 2017, **321**, 44-54.
33. A. J. McCue, D. S. Urgast, R. P. K. Wells and J. A. Anderson, *Catal. Commun.*, 2014, **43**, 159-163.
34. A. Mathew, S. Parambadath, S. S. Park and C. S. Ha, *Microporous Mesoporous Mater.*, 2014, **200**, 124-131.
35. X. Xu, S. Lü, C. Gao, X. Wang, X. Bai, N. Gao and M. Liu, *Chem. Eng. J.*, 2015, **266**, 171-178.
36. B. González, M. Colilla, C. L. De Laorden and M. Vallet-Regí, *J. Mater. Chem.*, 2009, **19**, 9012-9024.
37. X. Chen and Z. Liu, *J. Mater. Chem. B*, 2016, **4**, 4382-4388.
38. D. Pan, C. Guo, K. Luo and Z. Gu, *Chin J Chem*, 2014, **32**, 27-36.
39. K. Landskron and G. A. Ozin, *Science*, 2004, **306**, 1529-1532.
40. B. Boury, R. J. P. Corriu and R. Nuñez, *Chem. Mater.*, 1998, **10**, 1795-1804.
41. J. W. Kriesel and T. D. Tilley, *Chem. Mater.*, 1999, **11**, 1190-1193.
42. G. Larsen, E. Lotero and M. Marquez, *J Phys Chem B*, 2000, **104**, 4840-4843.
43. G. Larsen, E. Lotero and M. Marquez, *Chem. Mater.*, 2000, **12**, 1513-1515.
44. B. K. Cho, A. Jain, S. Mahajan, H. Ow, S. M. Gruner and U. Wiesner, *J. Am. Chem. Soc.*, 2004, **126**, 4070-4071.
45. T. Magbitang, V. Y. Lee, J. N. Cha, H. L. Wang, W. R. Chung, R. D. Miller, G. Dubois, W. Volksen, H. C. Kim and J. L. Hedrick, *Angew. Chem. Int. Ed.*, 2005, **44**, 7574-7580.

46. G. J. D. A. A. Soler-Illia, L. Rozes, M. K. Boggiano, C. Sanchez, C. O. Turrin, A. M. Caminade and J. P. Majoral, *Angew. Chem. Int. Ed.*, 2000, **39**, 4250-4254.
47. J. G. Croissant, C. Qi, O. Mongin, V. Hugues, M. Blanchard-Desce, L. Raehm, X. Cattoën, M. Wong Chi Man, M. Maynadier, M. Gary-Bobo, M. Garcia, J. I. Zink and J. O. Durand, *J. Mater. Chem. B*, 2015, **3**, 6456-6461.
48. J. Alauzun, A. Mehdi, C. Reyé and R. J. P. Corriu, *Chem. Commun.*, 2006, DOI: 10.1039/b512537e, 347-349.
49. F. X. Zhu, W. Wang and H. X. Li, *J. Am. Chem. Soc.*, 2011, **133**, 11632-11640.
50. F. Gröhn, B. J. Bauer, Y. A. Akpalu, C. L. Jackson and E. J. Amis, *Macromolecules*, 2000, **33**, 6042-6050.
51. Y. G. Kim, S. K. Oh and R. M. Crooks, *Chem. Mater.*, 2004, **16**, 167-172.
52. K. Bürglová, A. Noureddine, J. Hodačová, G. Toquer, X. Cattoën and M. Wong Chi Man, *Chem. Eur. J.*, 2014, **20**, 10371-10382.
53. S. Shenoi-Perdoor, A. Noureddine, F. Dubois, M. Wong Chi Man and X. Cattoën, in *Handbook of Sol-Gel Science and Technology: Processing, Characterization and Applications*, Springer International Publishing, 2018, DOI: 10.1007/978-3-319-32101-1_95, pp. 3001-3040.
54. B. Arunachalam, U. T. Phan, H. J. Geuze and P. Cresswell, *PROC. NATL. ACAD. SCI. U. S. A.*, 2000, **97**, 745-750.
55. D. Zhang, A. Fourie-O'Donohue, P. S. Dragovich, T. H. Pillow, J. D. Sadowsky, K. R. Kozak, R. T. Cass, L. Liu, Y. Deng, Y. Liu, C. E. C. A. Hop and S. Cyrus Khojasteh, *Drug Metab. Dispos.*, 2019, **47**, 1156-1163.
56. G. Gasquères, C. Bonhomme, J. Maquet, F. Babonneau, S. Hayakawa, T. Kanaya and A. Osaka, *Magn. Reson. Chem.*, 2008, **46**, 342-346.
57. F. Dogan, C. Joyce and J. T. Vaughey, *J Electrochem Soc*, 2013, **160**, A312-A319.
58. E. B. Cho, D. Kim and M. Jaroniec, *J. Phys. Chem. C*, 2008, **112**, 4897-4902.
59. P. K. Maiti, T. Çağin, G. Wang and W. A. Goddard III, *Macromolecules*, 2004, **37**, 6236-6254.
60. D. A. Tomalia, A. M. Naylor and W. A. Goddard, III, *Angew. Chem. Int. Ed. Engl.*, 1990, **29**, 138-175.
61. P. Trens, N. Tanchoux, A. Galarneau, D. Brunel, B. Fubini, E. Garrone, F. Fajula and F. Di Renzo, *Langmuir*, 2005, **21**, 8560-8564.
62. K. J. Shea, D. A. Loy and O. Webster, *J. Am. Chem. Soc.*, 1992, **114**, 6700-6710.
63. A. S. Lee, S.-S. Choi, K.-Y. Baek and S. S. Hwang, *Inorg. Chem. Commun.*, 2016, **73**, 7-11.
64. C. M. V. Stålhandske, C. I. Stålhandske, I. Persson, M. Sandström and F. Jalilehvand, *Inorg. Chem.*, 2001, **40**, 6684-6693.
65. R. C. Elder, K. Ludwig, J. N. Cooper and M. K. Eidsness, *J. Am. Chem. Soc.*, 1985, **107**, 5024-5025.
66. H. Qian, W. T. Eckenhoff, Y. Zhu, T. Pintauer and R. Jin, *J. Am. Chem. Soc.*, 2010, **132**, 8280-8281.
67. T. Bürgi, *Nanoscale*, 2015, **7**, 15553-15567.
68. M. Zhu, W. T. Eckenhoff, T. Pintauer and R. Jin, *J. Phys. Chem. C*, 2008, **112**, 14221-14224.
69. M. Zhu, C. M. Aikens, F. J. Hollander, G. C. Schatz and R. Jin, *J. Am. Chem. Soc.*, 2008, **130**, 5883-5885.
70. Y. Goto and S. Inagaki, *Chem. Commun.*, 2002, **2**, 2410-2411.
71. M. Laird, C. Carcel, E. Oliviero, G. Toquer, P. Trens, J. R. Bartlett and M. Wong Chi Man, *Microporous Mesoporous Mater.*, 2020, **297**, Article 110042.
72. Y. Guari, C. Thieuleux, A. Mehdi, C. Reyé, R. J. P. Corriu, S. Gomez-Gallardo, K. Philippot and B. Chaudret, *Chem. Mater.*, 2003, **15**, 2017-2024.
73. F. Kerdi, V. Caps and A. Tuel, *Microporous Mesoporous Mater.*, 2011, **140**, 89-96.
74. E. Besson, A. Mehdi, C. Reyé and R. J. P. Corriu, *J. Mater. Chem.*, 2009, **19**, 4746-4752.
75. L. Li, X. Wang, J. Yang, X. Ye and C. Wu, *Macromolecules*, 2014, **47**, 650-658.
76. V. Weiss, C. Argyo, A. A. Torrano, C. Strobel, S. A. Mackowiak, A. Schmidt, S. Datz, T. Gatzenmeier, I. Hilger, C. Bräuchle and T. Bein, *Microporous Mesoporous Mater.*, 2016, **227**, 242-251.
77. A. Birault, E. Molina, C. Carcel, J. Bartlett, N. Marcotte, G. Toquer, P. Lacroix-Desmazes, C. Gérardin and M. Wong Chi Man, *J Sol Gel Sci Technol*, 2019, **89**, 189-195.
78. A. Bondi, *Journal of Physical Chemistry*, 1964, **68**, 441-451.
79. Y. H. Zhao, M. H. Abraham and A. M. Zissimos, *J. Org. Chem.*, 2003, **68**, 7368-7373.